IDEA League

Master of Science in Applied Geophysics

Research Thesis

Nanoseismics: Evaluating a 3D Ultrasonic Instrument for Concrete

Di Wu

October 27, 2023

Nanoseismics: Evaluating a 3D Ultrasonic Instrument for Concrete

Master of Science Thesis

for the degree of Master of Science in Applied Geophysics
by

Di Wu

October 27, 2023

IDEA LEAGUE
JOINT MASTER'S IN APPLIED GEOPHYSICS

Delft University of Technology, The Netherlands
ETH Zürich, Switzerland
RWTH Aachen, Germany

Dated: *October 27, 2023*

Supervisor(s):

Ernst Niederleithinger

Vera Lay

Committee Members:

Ernst Niederleithinger

Deyan Draganov

Eidesstattliche Versicherung

Wu, Di	438504
Name, Vorname	Matrikelnummer (freiwillige Angabe)

Ich versichere hiermit an Eides Statt, dass ich die vorliegende Arbeit/Bachelorarbeit/ Masterarbeit* mit dem Titel

Nanoseismics: Evaluating a 3D Ultrasonic Instrument for Concrete

selbständig und ohne unzulässige fremde Hilfe erbracht habe. Ich habe keine anderen als die angegebenen Quellen und Hilfsmittel benutzt. Für den Fall, dass die Arbeit zusätzlich auf einem Datenträger eingereicht wird, erkläre ich, dass die schriftliche und die elektronische Form vollständig übereinstimmen. Die Arbeit hat in gleicher oder ähnlicher Form noch keiner Prüfungsbehörde vorgelegen.

Berlin, 27-10-2023	
Ort, Datum	Unterschrift

*Nichtzutreffendes bitte streichen

Belehrung:

§ 156 StGB: Falsche Versicherung an Eides Statt

Wer vor einer zur Abnahme einer Versicherung an Eides Statt zuständigen Behörde eine solche Versicherung falsch abgibt oder unter Berufung auf eine solche Versicherung falsch aussagt, wird mit Freiheitsstrafe bis zu drei Jahren oder mit Geldstrafe bestraft.

§ 161 StGB: Fahrlässiger Falscheid; fahrlässige falsche Versicherung an Eides Statt

(1) Wenn eine der in den §§ 154 bis 156 bezeichneten Handlungen aus Fahrlässigkeit begangen worden ist, so tritt Freiheitsstrafe bis zu einem Jahr oder Geldstrafe ein.

(2) Straflosigkeit tritt ein, wenn der Täter die falsche Angabe rechtzeitig berichtigt. Die Vorschriften des § 158 Abs. 2 und 3 gelten entsprechend.

Die vorstehende Belehrung habe ich zur Kenntnis genommen:

Berlin, 27-10-2023	
Ort, Datum	Unterschrift

Abstract

Ultrosonic pulse-echo testing is gaining increasing attention for its feasibility, accuracy, and versatility in structural examinations of concrete constructions. A1040 MIRA 3D PRO is an emerging low-frequency pulse-echo ultrasonic tomography device. Developed in 2021, this device is claimed to be suitable for manual and automated concrete structure assessment with the help of its functions, such as 3D-TFM (Total Focusing Method)/FMC (Full Matrix Capture) imaging. However, both its capacity and limitations need to be investigated in more detail. In this thesis, experiments are conducted first on a 2D concrete structure to examine the data acquired when the transducers are working in linear configuration and matrix configuration (array modes). Then, measurements were carried out on a 3D concrete structure to check the 3D properties of the device with the help of the data processing software InterSAFT. The results show a good correspondence between different array modes and that 3D SAFT could visualize 3D structures in an adjacent position. The data recorded at a greater distance was overlaid by noise, which is attributed to the fact that the frequency of the ultrasonic waves was set too high. Finally, further experiments on frequency calibration, data comparison, and measurements on more complicated specimens were suggested for future research on MIRA 3D PRO.

Acknowledgements

I would like to devote my thanks first to my supervisors, Dr. Ernst Niederleithinger and Dr. Vera Lay, for their expertise, guidance, and support during my experience working and studying at BAM.

Then, I would also like to thank all the colleagues that I collaborated with at Division 8.2, including Thomas Kind, Christoph Strangfeld, Jens Wöstmann, Marco Lange, and Ute Antonie Effner.

Thanks to Mr. Klaus Mayer for his instructions and help with the software.

A special thanks to my friend Lingshan Xiong, who is always there to support me during my thesis project.

I would also like to say thank you to my parents for all the love and support.

BAM, Berlin Di Wu
October 27, 2023

Table of Contents

Abstract vii

Acknowledgements ix

Nomenclature xvii

Acronyms xvii

1 Introduction 1

2 Method 5

2-1 Theory . . . 5

2-1-1 Ultrasonics and seismics . . . 5

2-1-2 Synthetic Aperture Focusing Techniques (SAFT) . . . 7

2-2 Hardware . . . 8

2-2-1 Introduction . . . 8

2-2-2 Geometry . . . 9

2-2-3 Technical Properties . . . 10

2-2-4 Array Modes . . . 11

2-3 Software . . . 12

3 Experiments on 2D Structures 13

3-1 Specimen . . . 13

3-2 Experiments . . . 15

3-2-1 Noisy Trace Testing . . . 15

3-2-2 Frequency Analysis . . . 16

3-2-3 B-scan Comparison . . . 19

4 Experiments on 3D Structures **21**
4-1 Specimen . . . 21
4-2 Experiments . . . 21
4-2-1 Data Preparation . . . 23
4-2-2 2D SAFT . . . 28
4-2-3 3D SAFT . . . 28
4-3 Results . . . 29
4-3-1 2D SAFT . . . 29
4-3-2 3D SAFT . . . 30

5 Discussion **35**

Bibliography **37**

A **39**
A-1 Codes and Scripts . . . 39
A-1-1 An appendix subsection with Python Lisitng . . . 39
A-1-2 A MATLAB Listing . . . 41

B **43**
B-1 A Brief Manual on MIRA 3D and InterSAFT . . . 43

List of Figures

1-1 The 2D ultrasonic echo instrument A1040 MIRA, consists of 12 linear arrays with 4 transducers of each [ACS, 2018]. . . . 2

2-1 Ultrasonic B-scan images a) before and b) after reconstruction by 2D synthetic aperture focusing technique (SAFT) [Schickert et al., 2003]. . . . 8

2-2 The top and bottom surfaces of ACS A1040 MIRA 3D PRO, with two basic units (the *master* and *slave*) and the controlling tablet connected wirelessly [ACS, 2022a]. 9

2-3 Transducer array geometry and naming of ACS A1040 MIRA 3D PRO. The two basic units are in total equipped with $4 \times 16 = 64$ piezoelectric transducers, named from 0101 to 1604. Each transducer is an individual pulser-receiver [ACS, 2022b]. Sketch provided by Vera Lay. . . . 10

2-4 B-scan view on ACS A1040 MIRA 3D PRO control unit (on the screen of the controlling tablet). The first (1), second (2), and third back-wall (3) echos are well recognizable [ACS, 2022b]. . . . 11

2-5 Icons of softwares used in this thesis, namely InterSAFT, Spydere (Python 3.11), and Matlab R2022a. . . . 12

3-1 Photo of the concrete specimen Pk266. . . . 14

3-2 Sketch of the front view of concrete specimen Pk266. It has four steps with thicknesses of 570, 450, 330, and 210 mm respectively. The width of these four steps are all 500 mm, with the tendon ducts at the center of each width. The thichness of the entire specimen is 800 mm. Sketch made by Martin Krause at BAM. . . . 14

3-3 Sketch of the 3D view of the concrete specimen Pk266. Sketch made by Martin Krause at BAM. . . . 15

3-4 Photo of the device position for noise trace testing . . . 16

3-5 Photo of the device position for noise trace testing . . . 17

3-6 The frequency spectrum of the matrix data. The figure on the upper left is an example A-scan, under the filter depicted in the upper right figure, the filtered A-scan is shown in the figure on the lower left, with its frequency spectrum on the lower right. . . . 17

3-7 The SAFT reconstruction (a) without filtering and (b) with a band-pass filter at 0-100 kHz. Image is produced with the magnitude of the reconstruction data to better present the structure of the tendon ducts and backwalls. After band-pass filtering, the noisy fringes in the image are effectively eliminated. 18

3-8 The InterSAFT reconstruction result from a)Linear Mode data, b)Matrix Mode compressed to linear data, c)Matrix Mode data (all normalized. Sub-figure d) is the difference between a and b, showing random noise in the figure without the target structure (bottom steps and the tendon ducts), suggesting that there is a good accordance between two modes. 19

4-1 Sketch of specimen Pk264 (front view). The measurement grid covers the rectangle marked in brown, the entire aperture of the Matrix Mode measurement is marked in red. Modified by the sketch from Stefan Maack at BAM. 22

4-2 Sketch of specimen Pk264 (top view). Made by Stefan Maack at BAM. 22

4-3 Because part of the device is out of the specimen for the first two columns of the measurement points, there are traces full of noise and do not provide any information about the specimen (as explained in chapter 3). This would influence the S/N of the final SAFT reconstruction. 23

4-4 One measurement at array position (4, 5) was selected for data checking. 24

4-5 2D SAFT reconstructions ot three A-scans selected in Figure 4-4 are shown in the same plot. It is clear that the A-scan on the left has the largest amplitude, which is anticipated to be caused by the energy reflected by the side wall of Pk264. . . 25

4-6 A Band-pass filter with cutoff frequencies at 0 and 140 kHz. Some high-frequency noises are filtered out, improving the S/N ratio for further processing. 26

4-7 A gain function was applied to suppress the shallow arrivals and visualize more details from larger depths. 26

4-8 After the band-pass filter and gain function are implemented, signals from structures in the specimen are more visually recognizable. For example, the reflection at about 3×10^{-4} s is clear, which is interpreted as the signal reflected from the backwall of Pk264. 27

4-9 The row of measuring positions for 2D SAFT, with the extended geometry due to the aperture of the device. 28

4-10 The 2D SAFT reconstructions at measuring row 5 (a)with and (b)without a band-pass filter applied at 0-140 kHz. This x-z slice is right crossing styrofoam ball 1. 29

4-11 The 2D SAFT reconstructions at measuring row 11 (a)with and (b)without a bandpass filter applied at 0-140 kHz. This x-z slice is right crossing styrofoam ball 6. 30

4-12 The 3D SAFT reconstructions at (a)measuring row 5 and (b)measuring row 11 with a bandpass filter applied at 0-140 kHz. The data used for 3D SAFT is from measurement row 5 and 11 respectively. This x-z slice is right crossing styrofoam ball 1 and 2. 31

4-13 The 3D SAFT reconstructions at (a)measuring row 5 and (b)measuring row 11 from the entire data set, with a bandpass filter applied at 0-140 kHz. 31

4-14 (a)x-y slice of the 3D SAFT reconstructions at the depth of z = - 158 mm, and (b)the measurement positions where the data was used for 3D SAFT reconstruction. Red circle denotes ball 1 and white circle denotes ball 6. Only a limited data set near the position of the balls were used. 33

4-15 (a)x-y slice of the 3D SAFT reconstructions at the depth of z = - 158 mm, and (b)the measurement positions where the data was used for 3D SAFT reconstruction. Red circle denotes ball 1 and white circle denotes ball 6. The entire data set were used for 3D SAFT reconstruction. 34

List of Tables

2-1 Terminology translation between engineering and geophysical context. The terms translated with each other can only be regarded as analogies. They are different concepts, some pairs with identical meaning while others are just defined based on similar theories [Wu, 2023]. 6

Acronyms

TUD Delft University of Technology, Netherlands

ETH Swiss Federal Institute of Technology, Switzerland

RWTH RWTH Aachen University, Germany

BAM Federal Institute of Materials Research and Testing (Germany)

Pk Specimen, "Probekörper" in German

SAFT Synthetic Aperture Focusing Technique

FMC/TFM Full Matrix Capture/Total Focusing Method

UPV Ultrasonic Pulse Velocity

UPE Ultrasonic Pulse-Echo

S/N Signal to Noise Ratio

Chapter 1

Introduction

Concrete is a complex quasi-brittle heterogeneous and anisotropic material that is produced by binding aggregates and cement paste [Jain et al., 2021]. It is widely used in civil and construction engineering, with an uneven nature to provide the necessary strength and durability for construction. To increase the strength of the concrete, reinforcement steel bars (rebars in short)are also added to the concrete mixture[Popovics and Rose, 1994]. It is mostly found in highways, building foundations, and concrete bridges. Even though the concrete mixture complies with conventional measurements, the quality of the source materials — such as sand, gravel, and cement — still varies. There is no standard model that accurately depicts a concrete block [Ahmad et al., 2014].

The purpose of quality control, structural assessment, reliable prolongation, and maintenance of the operational service life of the current concrete structure have become major issues. To effectively achieve these goals, a variety of tests are carried out to better parameterize and characterize the concrete structures [Jain et al., 2021], such as density, elastic modulus and strength and surface absorption, and the location and size of the reinforcement [Ahmad et al., 2014].

Non-destructive testing (NDT), which is carried out without destroying the structure of the investigated feature, is crucial for identifying inner items like defects, voids, delamination, and reinforcements in civil constructions to track their stability, duration, and attrition status [Niederleithinger et al., 2017].

Ultrasonic testing stands out among all the NDT techniques for its practicality and viability in concrete detection due to its fast measuring speed [Popovics, 2005], high accuracy [Ahmad et al., 2014], versatility [FPrimeC, 2017], and ease of use at a reasonable cost [JAIN and Patankar, 2019]. The application of ultrasonic testing in concrete investigations dates back several decades, and its initial usage was restricted to Ultrasonic Pulse Velocity (UPV) measurements in transmission mode for concrete quality control. Since the late 1990s, the one-sided access method - echo techniques, i.e. Ultrasonic Pulse–Echo (UPE) techniques, have gained increasing attention for structural examinations of concrete constructions [Niederleithinger et al., 2019].

Figure 1-1: The 2D ultrasonic echo instrument A1040 MIRA, consists of 12 linear arrays with 4 transducers of each [ACS, 2018].

Over the past two decades, there have been significant advancements in ultrasonic echo instrumentation for concrete testing. These instruments, primarily based on shear wave point contact transducers, have been developed to increase power and sensitivity, prevent data loss, and improve directionality and averaging. These arrays are used in single-channel instruments, while more sophisticated devices, such as linear arrays (see Figure 1-1) or tomographs, have 8 to 16 arrays each with 3 to 4 transducers, allowing multiple measurements in one go. However, for larger investigation areas or complex testing tasks, multiple measurements still need to be taken and combined [Niederleithinger et al., 2019].

Recent developments of the ultrasonic echo method include additional data capabilities, such as online storage to cloud systems or full matrix capture using every transducer as a separate unit. Additionally, augmented reality has been used for the display of results. Despite these advancements, there are still some drawbacks of this technique, including a limited penetration depth of up to 1 m, lack of resolution for sub-cm structures, and limitations in imaging complex structures or diffuse damages [Niederleithinger et al., 2019].

Among diverse choices of portable ultrasonic imaging devices for concrete detection, there appears one low-frequency pulse-echo ultrasonic tomography device named A1040 MIRA 3D PRO, which is a commercial ultrasonic tomographic system produced by ACS (Acoustic Control Systems) Group, Ltd. Developed in 2021, this emerging device is described to be suitable for manual and automated assessment of concrete structures, such as the localization of reinforcement rebars and other elements, the detection of material voids, and the measurement of thickness by one-side access [ACS, 2022a].

With an extended measuring aperture and special transmitting techniques, as well as the ability to perform 3D-TFM (Total Focusing Method) imaging, A1040 MIRA 3D PRO is anticipated to have promising utilization on concrete detection [ACS, 2022a].

Before this is truly accomplished, however, both the capability and limitations of this device still need to be examined and characterized independently in more detail. In this sense, a series of questions remain to be addressed. For example, compared to its predecessor A1040

MIRA, whether and how its imaging resolution is improved, how much its inspection range, especially penetration depth, is increased, to what extent its flaw detectability is enhanced, and how effectively the three-dimensional FMC (Full Matrix Capture)/TFM (Total Focus Method) in each instrument position is implemented.

In order to have a further understanding of the potential and limitations of A1040 MIRA 3D PRO, in this thesis, a series of experiments and analyses were carried out in the laboratory and the office.

In Chapter 2, basic theories such as the synthetic aperture focusing technique (SAFT), the property of the hardware MIRA 3D PRO, and the data processing software InterSAFT were introduced.

Then in Chapter 3, experiments were designed and conducted on a 2D concrete structure, during which the data sorting order, A-scans, and frequency spectrum of the data from the device were examined. An appropriate band-pass filter was designed to enhance imaging. Data acquired in Linear and Matrix Array Modes was tested and compared.

In Chapter 4, the device was used for the experiments carried out on a 3D concrete structure so that its 3D performance could be investigated. In this chapter, the reconstruction of A-scans was checked, the band-pass filter was redesigned for the corresponding operation frequency and specimen, and the gain function was manually designed to enhance deeper signals. After these data preparation procedures, 2D and 3D SAFT were performed and investigated.

Finally in Chapter 5, the experiments and their results are discussed and concluded, with an outlook on MIRA 3D PRO and relative techniques provided.

Chapter 2

Method

2-1 Theory

2-1-1 Ultrasonics and seismics

There are many similarities between Non-destructive testing (NDT) of concrete and geophysical surveys of the subsurface of earth. Some techniques such as ground penetrating radar (GPR), are commonly applied in both contexts. In other cases, some methods in both fields are developed based on similar principles, for example, ultrasonic imaging in NDT and seismic surveys in geophysics both rely on the principles of mechanical wave propagation.

In both senses of ultrasonic imaging and seismic survey, waves (ultrasonic waves for ultrasonic imaging, seismic waves for seismic surveys) are sent into a material (concrete or earth) and propagate within it. Then the returning waves are received, processed, and analyzed to obtain information about the internal structures or properties of the medium being studied. Thus, the basic theories and data processing procedures for seismics could also be analogized in ultrasonic imaging, especially in ultrasonic pulse echo (UPE) testing, as the signal of interest is mainly the reflected waves from the target. Table 2-1 provides a common terminology translation between fields of engineering and geophysics, for readers with geophysical backgrounds to better get familiar with the NDT context.

According to the theory of elastic waves, if a mechanical wave encounters a sub-interface with a difference in elastic wave impedance in the propagation process, reflection and transmission will occur at the same time, resulting in reflected and transmitted waves, respectively. The energy distribution of the reflected and transmitted waves is related to the elastic wave impedance of the medium on both sides of the interfaces. The elastic impedance is defined as $Z = \rho v$, which is the product of a medium's sound propagation velocity v and its density ρ. When the elastic wave is injected from medium 1 perpendicularly to an interface into medium 2, the amplitude ratio of the reflected wave to the incident wave is called the reflection coefficient R and it is described in Equation 2-1.

$$R = \frac{Z_2 - Z_1}{Z_2 + Z_1} \qquad with \quad Z = \rho \cdot v \tag{2-1}$$

No.	Engineering Term	Geophysical Term	Notes
1	A-scan	Seismic trace	
2	B-scan	Seismic (cross) section	
3	C-scan	horizontal section (time slice)	
4	Time of flight	travel time	
5	Aperture	Survey line (or area)	for 2D or 3D
6	Synthetic aperture focusing technique (SAFT)	Kirchhoff migration	
7	Sending transducer	Source	
8	Receiving accelerometer	Receiver (geophone)	Just one type of receiver
9	Pixel	Data point	A time point of a single trace or a spatial point in the cross section
10	Longitudinal wave	P-wave (pressure wave)	
11	Transverse wave	S-wave (shear wave)	
12	Pulse-echo method	Reflection seismic method	
13	Transmission technique	Transmission tomography	
14	Axial position (or depth)	Depth (in Z axis)	

Table 2-1: Terminology translation between engineering and geophysical context. The terms translated with each other can only be regarded as analogies. They are different concepts, some pairs with identical meaning while others are just defined based on similar theories [Wu, 2023].

According to Equation 2-1, when the mechanical wave is injected into an interface between two mediums, the larger the difference in wave impedance between the two media on both sides of the interface, the larger the absolute value of the amplitude of the reflected wave, and the more obvious the reflection event on the B-scans. Therefore, ultrasonic echo testing could be implemented to detect the existence and geometry of structures such as rebars and tendon ducts that have different impedance with the concrete, which is based on the same fundamental principle as reflection seismic surveys are implemented [SEG, 2020].

2-1-2 Synthetic Aperture Focusing Techniques (SAFT)

Ultrasonic reconstruction by the Synthetic Aperture Focusing Technique (SAFT) is an imaging method in ultrasonic pulse-echo (UPE) testing to investigate concrete elements and identify embedded objects. By coherent superposition, the algorithm of SAFT focuses ultrasonic signals that are reflected from the same object and received at multiple aperture points on their correct position [Schickert et al., 2003].

For the utilization of SAFT in UPE testing of concrete, The measurements are conducted on the surface of the concrete on a one- or two-dimensional grid, which is also called an aperture. To scan the grid, one or more transducers must be moved because transducers with the size of an entire aperture are unmanageable, which is similar to the roll-along acquisition in seismic surveys [Ashton et al., 1993]. With a divergence angle where the transmitted beam is propagating inside [Schickert et al., 2003], signals reflected from the same point inside the concrete can be received at many points in the aperture. Linear apertures result in two-dimensional images, while planar apertures lead to three-dimensional ones [Schickert, 2005].

The fundamental time-domain 3D SAFT algorithm for the reconstruction of a three-dimensional image volume $g(x_i, y_j, z_k)$ based on pulse-echo measurements $f(x'_m, y'_n, t_{mn})$ on a planar aperture is given Equation 2-2 and Equation 2-3.

$$g(x_i, y_j, z_k) = \frac{1}{MN} \sum_m \sum_n f(x'_m, y'_n, t_{mn}) \tag{2-2}$$

$$\text{where } t_{mn} = t_0 + \frac{2}{c_p} \sqrt{(x'_m - x_i)^2 + (y'_n - y_j)^2 + (z'_k)^2} \tag{2-3}$$

Here c_p is the velocity at which the ultrasonic wave is propagating in the medium (concrete). While t_0 is the zero-time correction value, which means the time that a pulse signal passes the measurement system alone before it is transmitted into the concrete [Schickert et al., 2003]. Then the 2D SAFT algorithm is produced when $y'_n = y_j = 0$, as shown in Equation 2-4 and Equation 2-5.

$$g(x_i, z_k) = \frac{1}{M} \sum_m f(x'_m, t_m) \tag{2-4}$$

$$\text{where } t_m = t_0 + \frac{2}{c_p} \sqrt{(x'_m - x_i)^2 + (z'_k)^2} \tag{2-5}$$

In the transmitter-receiver configurations, the time of flight of the signals reflected from every single point in the concrete can be calculated based on the geometric relationships between the reflector and the receiver, presuming that the pulse velocity within the concrete

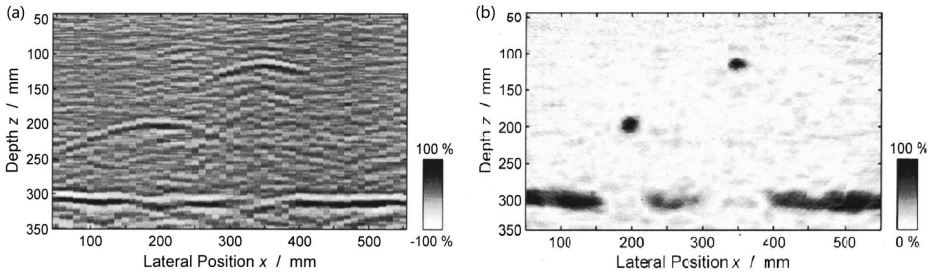

Figure 2-1: Ultrasonic B-scan images a) before and b) after reconstruction by 2D synthetic aperture focusing technique (SAFT) [Schickert et al., 2003].

is constant. Then, with increased spatial superposition, these signals can then be focused back on each pixel in the image, i.e., each spatial position in the concrete. As is revealed according to what has been explained, the basic principle behind SAFT is closely related to the seismic processing technique Kirchhoff Migration [Niederleithinger et al., 2017], which is also dispersing the signal energy in each trace over the corresponding semicircles (in 2D seismic sections) and then summing the contributions of all the seismic traces to each point in the subsurface [SEG, 2014].

Figure 2-1 shows two ultrasonic B-scan images before and after 2D SAFT reconstruction, respectively. It is clear that after the application of SAFT, the structural noise dispersed from the heterogeneous matrix and aggregates interferes destructively with each other, while the signals reflected from the target object boundaries interfere constructively. As a result, the pixels representing the object of interest are intensified and the structural noise is reduced, therefore the S/N ratio and spatial resolution of the generated image are enhanced [Schickert et al., 2003].

2-2 Hardware

2-2-1 Introduction

The hardware that is applied and examined in this thesis is the low-frequency pulse-echo ultrasonic tomography device **ACS A1040 MIRA 3D PRO** (MIRA 3D PRO in short), as is shown in Figure 2-2.

This instrument consists of two compact basic units and one control unit. Each of the basic units contains $8\times4 = 32$ Active Dry-Point-Contact (A-DPC) piezoelectric transducers with integrated pulser-receiver circuits and parallel data acquisition (DAQ) electronics [ACS, 2022a]. These transducers produce transverse waves (shear waves) that is polarized along the shorter axis of the instrument, i.e., $S_H - wave$, at a frequency range from 10 to 100 kHz. As mechanical waves may perform "mode conversion" when the direction of the polarization is discomposed and the wave mode may be converted, for example from $P - wave$ to secondary P-wave and $S_V - wave$, or from $S_V - wave$ to secondary $S_V - wave$ and P-wave. But since $S_H - wave$ is perpendicular to both the ray path direction and the incident and reflecting plane, it will not be converted so could contain its wave mode, making the received signal easier to process [Niederleithinger et al., 2017]. To increase the measuring aperture, the two

Figure 2-2: The top and bottom surfaces of ACS A1040 MIRA 3D PRO, with two basic units (the *master* and *slave*) and the controlling tablet connected wirelessly [ACS, 2022a].

basic units are physically assembled along their long side, therefore the entire device consists of $16 \times 4 = 64$ transducers.

The control unit, which is a tablet device, is equipped with parallel graphic processors to implement image reconstruction and visualization algorithms [ACS, 2022b]. It also has an Android operation system with an application named MIRA 3D installed for measurement settings and operations.

When the measurement is ongoing, the controlling tablet can be either attached to the basic units magnetically or placed separately (such as on a table). The control unit and two basic units are wirelessly connected to each other while working, and the two units function as so-called master and slave, or primary and secondary units.

2-2-2 Geometry

Figure 2-3 shows a sketch of the geometry and naming of the transducer array of MIRA 3D PRO in a top view. As aforementioned, the device contains 64 transducers in 16 columns and 4 rows, with a constant transducer interval of 25 mm in both x and y directions. Therefore the whole transducer array has the geometry of

$$(25\ mm \times 15) \times (25\ mm \times 3) = 375\ mm \times 75\ mm.$$

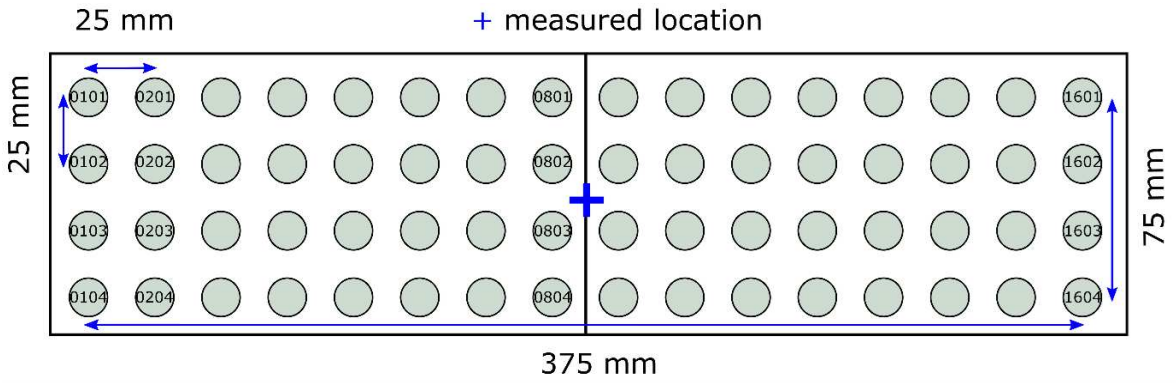

Figure 2-3: Transducer array geometry and naming of ACS A1040 MIRA 3D PRO. The two basic units are in total equipped with $4 \times 16 = 64$ piezoelectric transducers, named from 0101 to 1604. Each transducer is an individual pulser-receiver [ACS, 2022b]. Sketch provided by Vera Lay.

The transducers are named and numbered according to their row and column positions. In the top view of the transducer array (the side with the power keys of the units at the bottom), the transducer in the upper left is numbered 0101, and in the same row there are 0201, 0301,..., 1601 to the right end. Then in the second row from the left, the transducers are 0102, 0202,..., 1602. Finally, the one at the lower right corner is named Transducer 1604. The claimed measuring location is at the center of the transducer array, which is at $(187.5mm, -37.5mm)$ relative to Transducer 0101.

2-2-3 Technical Properties

ACS A1040 MIRA 3D PRO has four major display views while working, which are A-scan, B-scan, C-detect, and Map. For A-scan view, the A-scans from selected source and receiver transducer pairs are displayed for data checking before the measurements commence. In this view, the analog and digital gain can be tested and determined for optimal display amplitude. While one measurement is finished, MIRA 3D PRO can produce a preliminary reconstruction B-scan image and present it in the B-scan view. This function provides convenience for people operating the device so that they can check the data quality and target concrete property such as backwall reflection directly on site (see Figure 2-4). If a 2D aperture is designed for a 3D data volume and 3D image, the Map view is in use, where the x- and y-intervals of the aperture can be easily set. Together With the preset transverse ultrasonic velocity of the target concrete, the device could present the preliminary reconstruction truthfully. Additionally, the C-detect view is designed especially to detect cracks (especially those vertical to the measuring surface) in the concrete that are hard to capture in the normal B-scan mode.

The frequency of the pulse applied to the DPC (Dry-Point-Contact) -transducer of MIRA 3D PRO is defined as the *Operation frequency*, which is ranging from 10 to 100 kHz. For in-lab concrete tests, the operation frequency around 50 kHz is usually selected, varying with the target depth and desired resolution [ACS, 2022b].

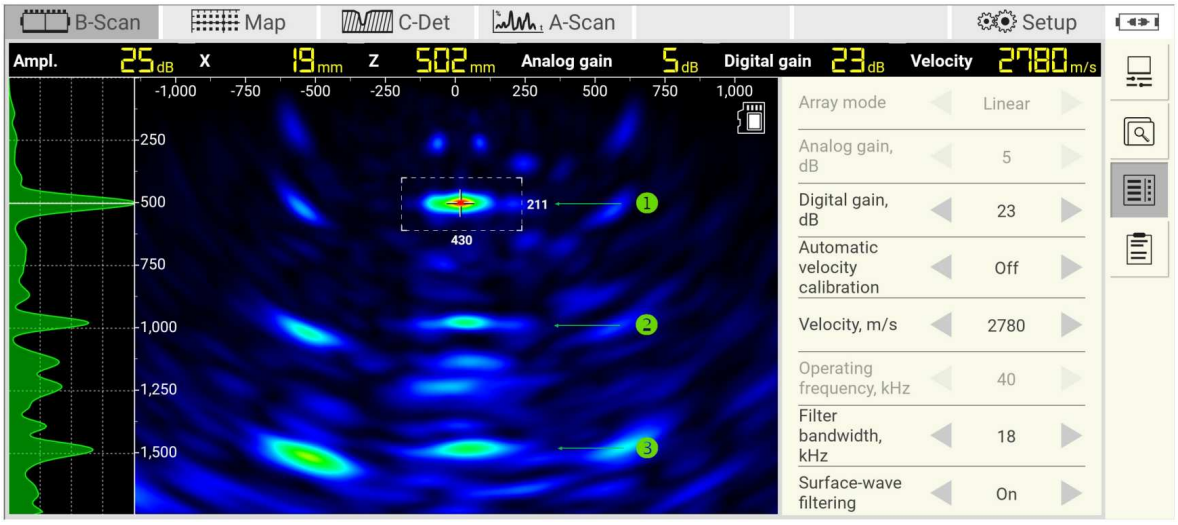

Figure 2-4: B-scan view on ACS A1040 MIRA 3D PRO control unit (on the screen of the controlling tablet). The first (1), second (2), and third back-wall (3) echos are well recognizable [ACS, 2022b].

2-2-4 Array Modes

One specialty of this newly emerging device is that the transducers can work independently in the whole array, forming a matrix of transducers instead of a line of transducer arrays in linear UPE devices, including its predecessor, the ACS A1040 MIRA. This is also where "3D" comes from in the name of the device, since this Full Matrix Capture (FMC)/Total Focusing Method (TFM) technique can contribute to a 3D image. To make use of this technique, the *Array mode* of the measurement needs to be set as Matrix, which means that the transducers are functioning as a matrix of individual sensors and the data is collected in Matrix Array Mode (Matrix Mode in short).

When the transducers are working in Matrix Mode, each of them can function either as a source or a receiver of the signal. During one measurement, transducer 0101 first works as the source and the rest 63 as receivers. Then the source switches to the right and transducer 0201 becomes the source. According to the principle of reciprocity, transducer 0101 will not receive the signal as the signal from 0101 and received by 0201 has already contains the same information of the measured concrete. Consequently there are 62 A-scans recorded when transducer 0201 is transmitting the signal. Then transducer 0301 acts as the source and 61 A-scans are recorded, and so on. After transducer 1601, it is transducer 0102's turn to transmit. In a similar fashion, finally transducer 1603 is the source and 1604 the only receiver. As a result, in Matrix Mode, there are $63 + 62 + 61 + ... + 1 = 2016$ A-scans recorded in one measurement.

On the contrary, in Linear Mode, each four transducers in the same column will function as one, transmitting or receiving the signal at the same time. In one measurement, array 1 (transducer 0101, 0102, 0103, and 0104, i.e. the first column of the sensors) first transmits signal and the other 15 arrays (sensor columns) receive. Then array 2 is the source and array 3 to 16 the receiver, till array 15 transmits and array 16 receives. Finally $15+14+13+...+1 = 120$ A-scans are recorded in Linear Mode and all of them are considered as received in the

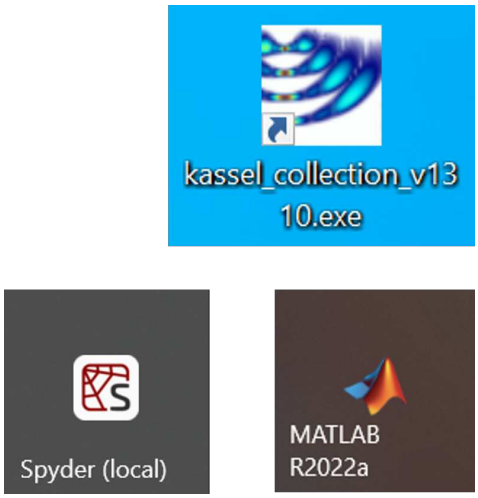

Figure 2-5: Icons of softwares used in this thesis, namely InterSAFT, Spydere (Python 3.11), and Matlab R2022a.

same line.

2-3 Software

The synthetic aperture focusing technique (SAFT) used for ultrasonic image reconstruction in this thesis, together with other processing methods such as bandpass filter, was carried out with the vendor-independent software InterSAFT from Dr.-Ing. Klaus Mayer from the University of Kassel [Mayer et al., 2008, Mayer and Cinta, 2012]. Some supportive processing works such as A-Scan plotting and comparison were carried out in Python 3.11 (Spyder), and B-Scan comparison with Matlab R2022a (see Figure 2-5).

Chapter 3

Experiments on 2D Structures

As A1040 MIRA 3D PRO is developed especially with the capability to implement three-dimensional FMC (Full Matrix Capture) / TFM (Total Focusing Method) in each instrument position [ACS, 2022a], its data property acquired in Matrix Mode first was reviewed and compared to that in Linear Mode. And a concrete specimen with a "2D structure" was selected under measurement. All the experiments carried out on this concrete specimen with a 2D structure and corresponding analyses are included in this chapter.

3-1 Specimen

The experiments introduced in this chapter were carried out on the specimen "Pk266" (Probekörper (Pk) in German means "specimen") of the Federal Institute of Materials Research and Testing (BAM) in Berlin, Germany [Maack et al., 2023]. A photo of this specimen is shown in Figure 3-1.

Pk266 is a concrete specimen mounted with four tendon ducts separately in four different thickness steps, with the upper surface flat where the testing instruments could be placed. As is shown in Figure 3-2, the thicknesses of these steps are 570, 450, 330, and 210 mm respectively. The width of these four steps are all 500 mm, and the horizontal position of the tendon ducts are at the center of each width of the steps.

Figure 3-3 also shows a 3D sketch of the concrete specimen Pk266. It is obvious from the geometry of Pk266 that this concrete specimen is mounted in a "2D way", which means little variation appears in the y-direction in the specimen. Therefore this specimen is suitable for the ultrasonic pulse-echo (UPE) testing experiments conducted to check the linear properties of the device.

The transverse ultrasonic velocity of Pk266 was set at 2800 m/s in the data peocessing in this chapter.

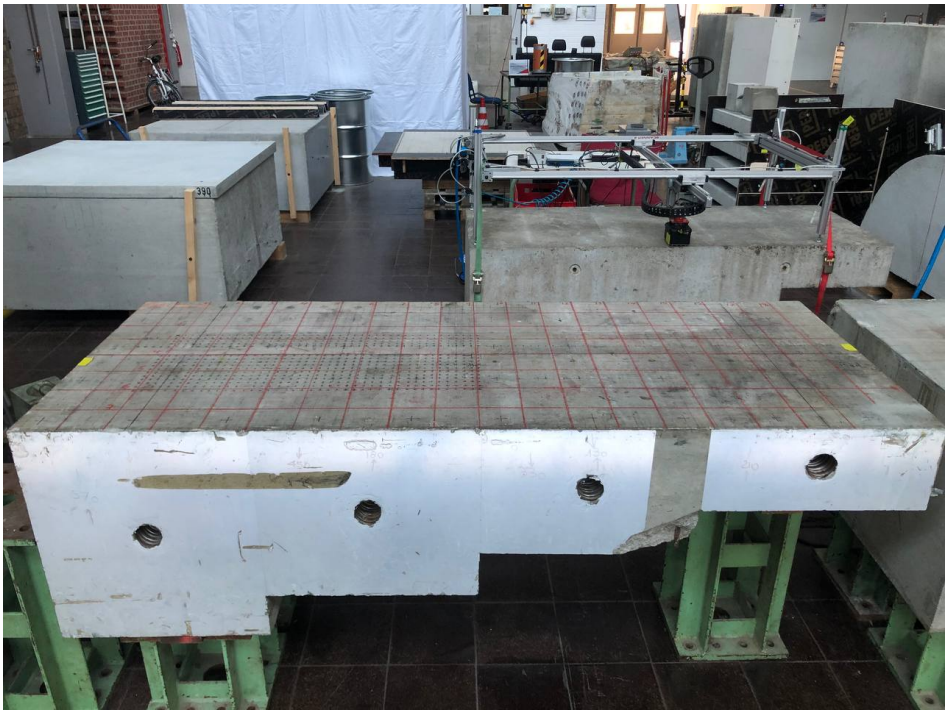

Figure 3-1: Photo of the concrete specimen Pk266.

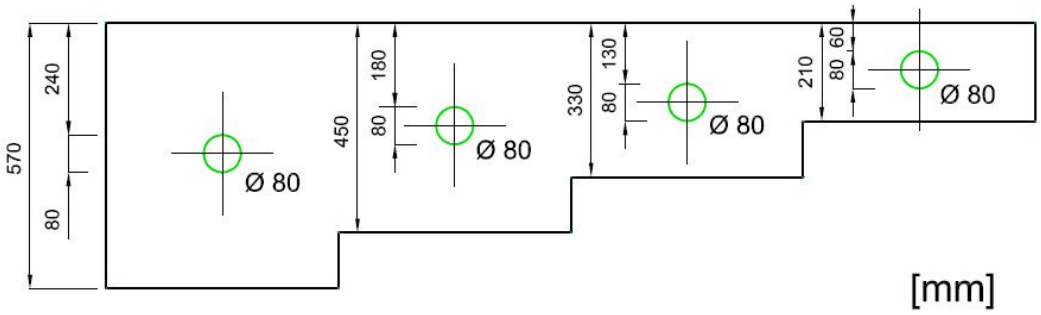

Figure 3-2: Sketch of the front view of concrete specimen Pk266. It has four steps with thicknesses of 570, 450, 330, and 210 mm respectively. The width of these four steps are all 500 mm, with the tendon ducts at the center of each width. The thichness of the entire specimen is 800 mm. Sketch made by Martin Krause at BAM.

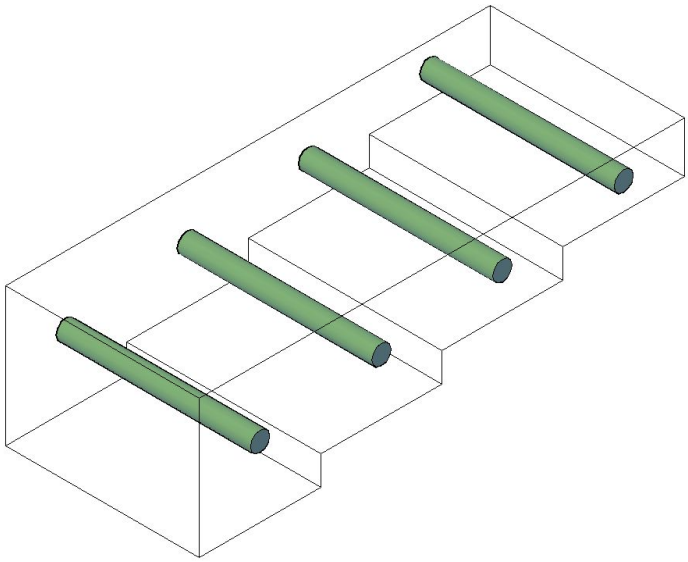

Figure 3-3: Sketch of the 3D view of the concrete specimen Pk266. Sketch made by Martin Krause at BAM.

3-2 Experiments

The UPE measurements introduced in this chapter was carried out on one measuring line (2D aperture) in the x-direction at y = 400 mm, i.e. at the center in y-direction, to obtain x-z slices of Pk266. In the measuring line, data were collected in 17 device positions, with an interval of 100 mm between each two positions, thus the total length of the measuring line is 1600 mm. The device was positioned parallel to the long side of the specimen. Considering the aperture of the device itself, the actual aperture of this measurement is 1600 + 375 mm = 1975 mm, which almost covers the full length of the Specimen (2000 mm).

With this design of measuring line, the measurement set with 17 device positions was carried out twice, only with Array Mode varies from linear for the first set and matrix for the second. All the other parameters and settings of these two sets of measurements were kept consistent. The operation frequency was set as 50 kHz, and the maximum "fold" of the data set is 16.

After the measurements, experiments on data processing was conducted including noise trace testing, A-scan comparison, frequency analysis, and B-scan comparison, to have a further understanding of the data.

3-2-1 Noisy Trace Testing

In the software InterSAFT, the data sorting direction could be set as "from left to right" or "from right to left", where the default setting is the former for MIRA 3D. To confirm this data sorting order as well as to recognize the noise traces in B-scans, a noisy trace testing was performed.

As shown in Figure 3-4, the noisy trace testing was conducted in Linear Mode by putting the device at the left edge of the specimen so that the four transducer arrays in the left was is

Figure 3-4: Photo of the device position for noise trace testing

suspended and thus not in contact with the specimen. In this way, the signals transmitted and received by these suspended arrays should be purely noisy and not containing any information of the specimen.

By calling browser on data in InterSAFT, the B-scan of raw data was displayed. As is shown in Figure 3-5, there are only 11 common source gathers visible in the right, indicating that the left four source gathers are contaminated by noise, which is consistent with the placement of the device while measuring. Therefore the default setting of the data sorting direction in InterSAFT is confirmed to be correct for MIRA 3D PRO data. This result could also help with recognizing the traces where the transducers are not well contacted with the specimen.

3-2-2 Frequency Analysis

Signal theory states that signals are periodic signals with different frequencies. By transforming arbitrary signals into the frequency domain, we can evaluate the energy proportion of each frequency. Frequency filters like low-pass, high-pass, and band-pass can eliminate undesirable data from certain frequency ranges, such as noise or device configuration, to increase useful signal content and improve data quality.

The claimed frequency of A1040 MIRA 3D PRO is 10 to 100 kHz [ACS, 2022b], and more details was reviewed. The signal quality should be improved as much as possible in order to suppress the noise; however, the filtering must not be overly aggressive in order to maintain the intended signal content.

After trying a series of values within the trade-off between suppressing the noise and keeping the desired signal content, a band-pass filter with the lower and upper cutoff frequency at 0 and 100 kHz respectively. Figure 3-6 shows the frequency spectrum of the matrix data with a central frequency of 50kHz. With the help of a band-pass filter of 0-100 kHz, the data can be effectively filtered and the Signal to Noise Ratio (S/N) of the SAFT reconstruction was be improved. As is shown in Figure 3-7, after the application of the band-pass filter, the noise fringes in the image, especially in the shallower depths are effectively eliminated.

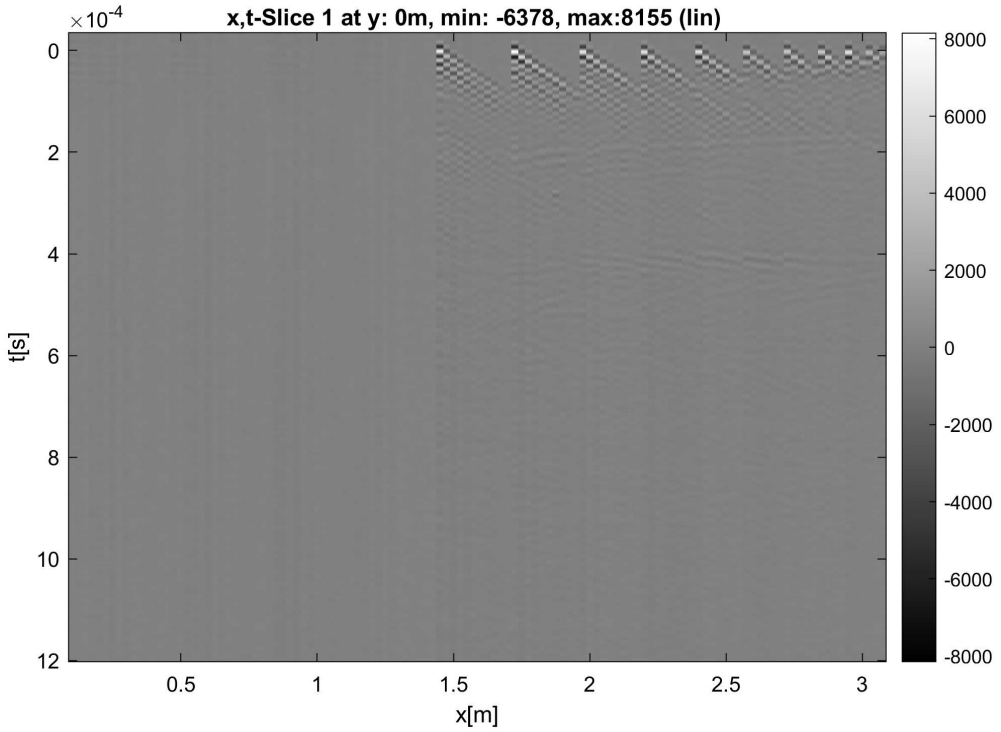

Figure 3-5: Photo of the device position for noise trace testing

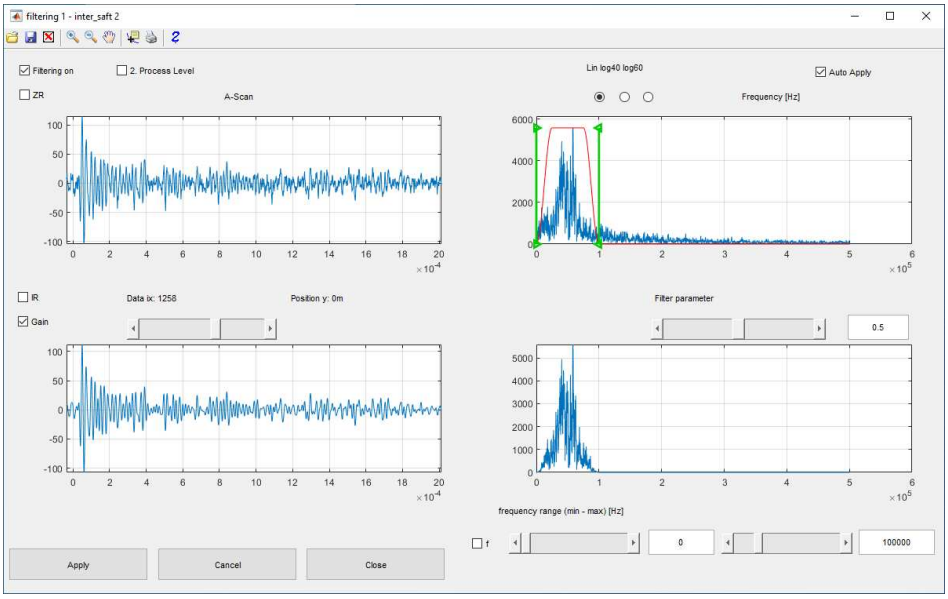

Figure 3-6: The frequency spectrum of the matrix data. The figure on the upper left is an example A-scan, under the filter depicted in the upper right figure, the filtered A-scan is shown in the figure on the lower left, with its frequency spectrum on the lower right.

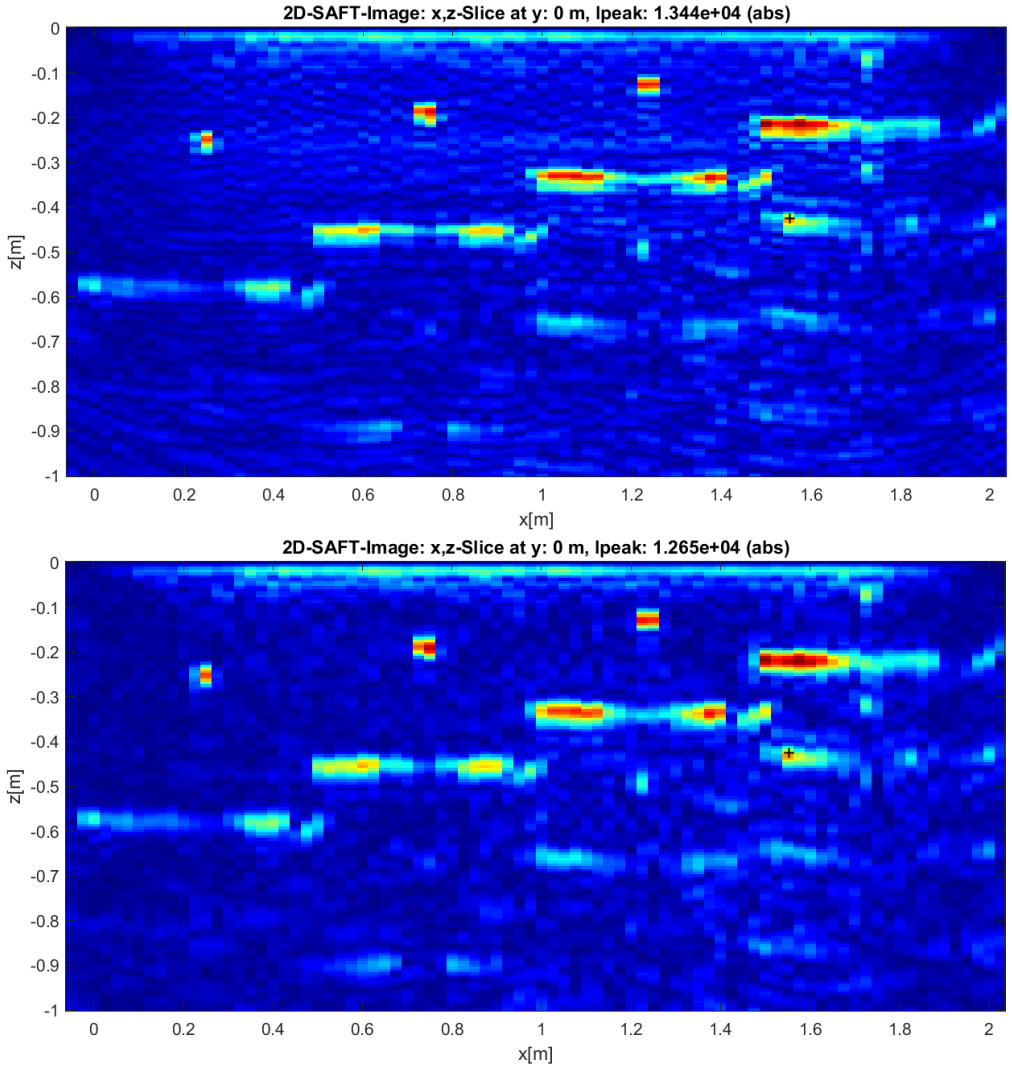

Figure 3-7: The SAFT reconstruction (a) without filtering and (b) with a band-pass filter at 0-100 kHz. Image is produced with the magnitude of the reconstruction data to better present the structure of the tendon ducts and backwalls. After band-pass filtering, the noisy fringes in the image are effectively eliminated.

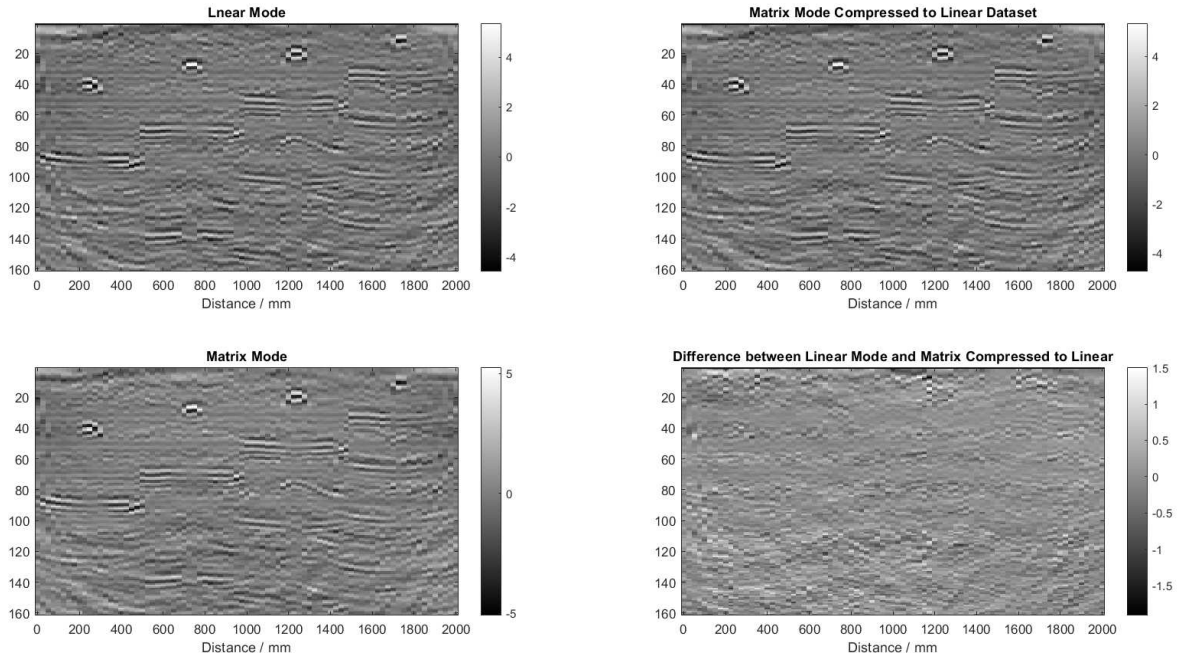

Figure 3-8: The InterSAFT reconstruction result from a)Linear Mode data, b)Matrix Mode compressed to linear data, c)Matrix Mode data (all normalized. Sub-figure d) is the difference between a and b, showing random noise in the figure without the target structure (bottom steps and the tendon ducts), suggesting that there is a good accordance between two modes.

3-2-3 B-scan Comparison

Their is an algorithm in InterSAFT that could compress the data acquired in matrix array mode along each column of the transducers, resulting in a new dataset that is stored, sorted, and presented the same as the data obtained in Linear Mode.

Therefore, except for the data in Linear Mode and Matrix Mode, there appears a third type of the data, those acquired in Matrix Mode while later compressed into a "linear mode" (compressed linear mode in short).

All of these three datasets were used for SAFT reconstruction, and the resulting images are first normalized and then shown in subfigures (a), (b), and (c) of Figure 3-8. For the reconstructions from Linear and Matrix Mode, the the normalized reconstructed data were also compared by subtracting the latter from the former. The result of this subtraction is also shown in subfigure (d). The images here are produced with the real part of the reconstruction data to better show the details of the structure, such as the first trigers.

According to Figure 3-8 (a), (b), and (c), the structures of the tendon ducts and backwalls are clearly presented in the reconstruction results from all three datasets. After subtracting (b) from (a), those structures all disappear, indicating that the 2D SAFT reconstructions from both Linear and Mtrix Mode data has a good consistency.

Chapter 4

Experiments on 3D Structures

4-1 Specimen

The experiments explained in this chapter were carried out on the specimen Pk264 of BAM. Pk264 is a concrete specimen sized 1800 mm × 900 mm × 380 mm , produced with 10 styrofoam balls and 17 reinforcement bars in it. The diameters of the balls in the upper row are 80 mm, and those in the lower row are 50 mm. All the big and small ball pairs in the y-direction are at different depths in the z-direction. The rebars are all along the y-direction, with 8 near the front wall and 9 in the back wall, all with diameters of 12 mm. The detailed information, including the geometry of the specimen and the size, location, and orientation of the styrofoam balls and rebars, is shown in Figure 4-1 and Figure 4-2.

The velocity was modified in multiple times to project the backwall echo at its true depth of 380 mm and the second echo (similar to multiple wave in seismics) at $380 \times 2 = 760\ mm$, and finally the transverse ultrasonic velocity of Pk266 was set at 2700 m/s for the data processing in this chapter.

4-2 Experiments

The measurement was designed to detect characterize styrofoam balls 1 and 6, where there is not any rebars over or behind these balls, providing a chance to examine the capability of MIRA 3D PRO to depict the true 3D structures.

The aperture of this measurement was designed on the front side of Pk264, directly over styrofoam ball 1 and ball 6, with 7 device positions in the x-direction and 15 in the y-direction. Both the x- and y- intervals are 50 mm. Thus, the size of the measuring grid is

$$(50\ mm \times 6) \times (50\ mm \times 14) = 30\ mm \times 70\ mm.$$

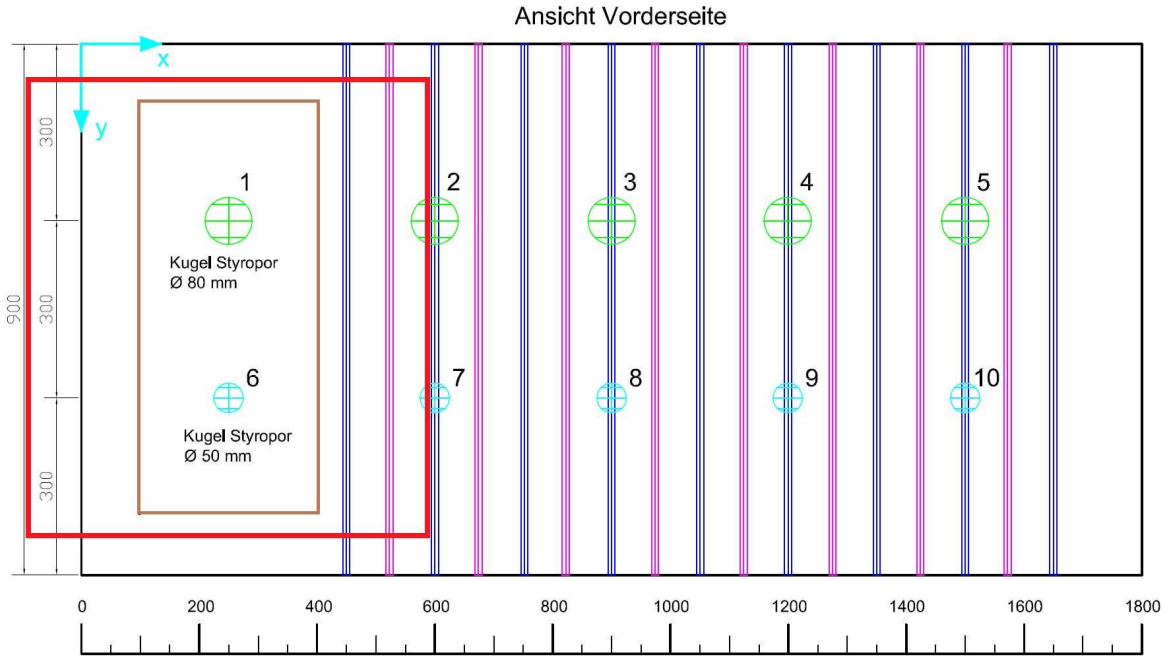

Figure 4-1: Sketch of specimen Pk264 (front view). The measurement grid covers the rectangle marked in brown, the entire aperture of the Matrix Mode measurement is marked in red. Modified by the sketch from Stefan Maack at BAM.

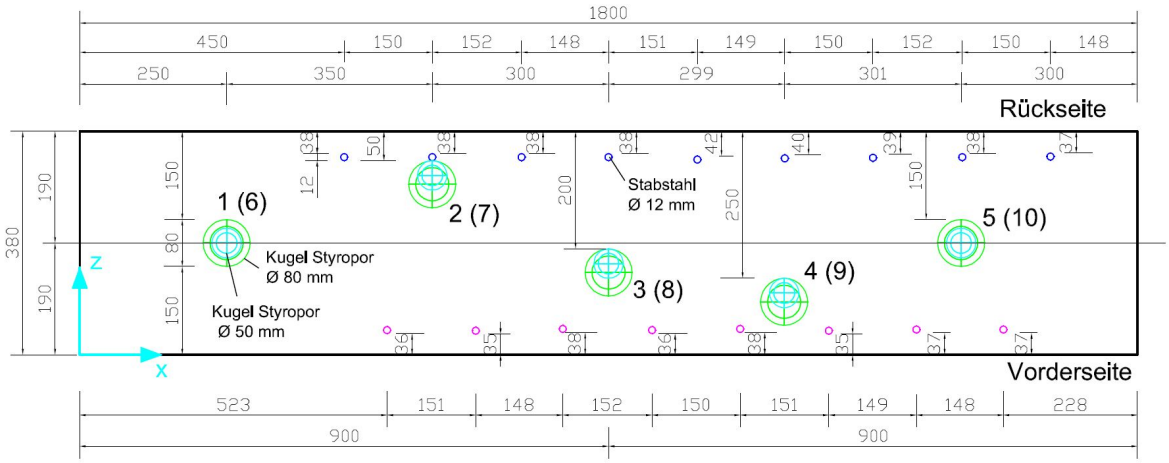

Figure 4-2: Sketch of specimen Pk264 (top view). Made by Stefan Maack at BAM.

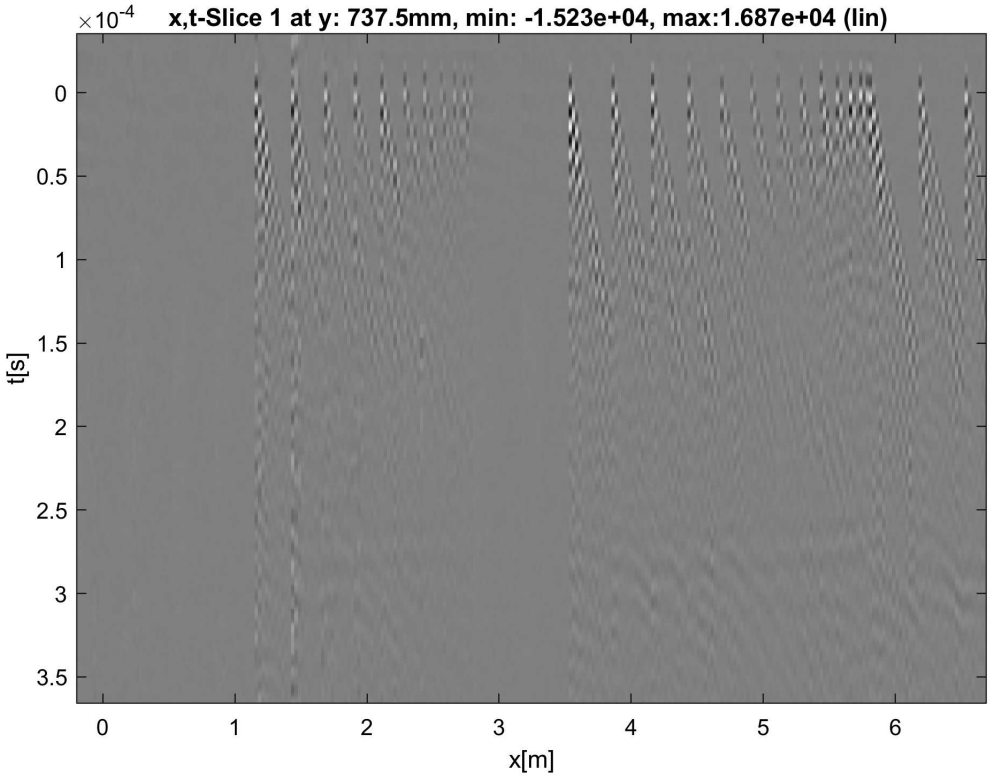

Figure 4-3: Because part of the device is out of the specimen for the first two columns of the measurement points, there are traces full of noise and do not provide any information about the specimen (as explained in chapter 3). This would influence the S/N of the final SAFT reconstruction.

Considering the geometry of the transducer array of the device, the actual area that the transducers cover is

$$(300 + 375\ mm) \times (700 + 75\ mm) = 675\ mm \times 775\ mm.$$

The left side of this aperture, as seen in Figure 4-1, extends beyond the left edge of the specimen. This indicates that, some transducer columns were suspended during the measurements on the left two columns in the measuring grid, as explained in chapter 3. The B-scan with the noisy traces resulting from this transducer suspension is shown in Figure 4-3.

The data was acquired in Matrix Mode, then a compressed linear mode dataset was also produced for comparison. Furthermore, a higher operation frequency of 75 kHz was chosen for use, as the targets of interest, the styrofoam balls, are at a shallower depth and with a smaller size compared to those in chapter 3.

4-2-1 Data Preparation

Before the actual processing, a compressed linear data set was produced from the original Matrix Mode data and was used to have a quick check of the properties of the data and to

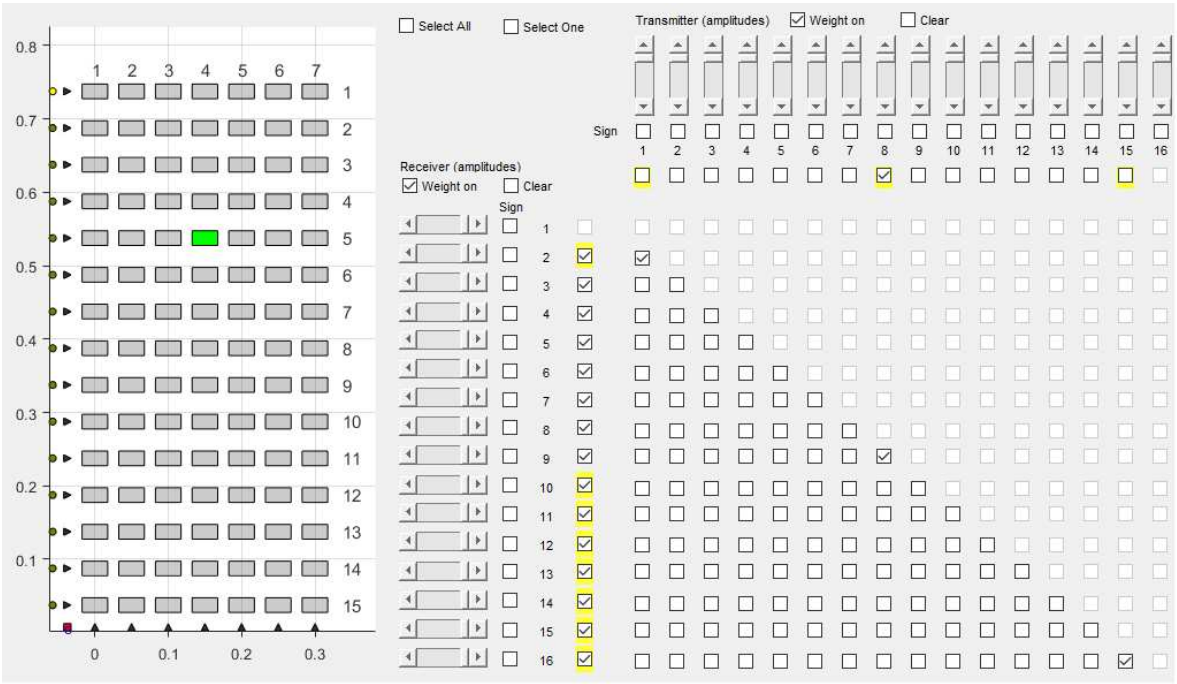

Figure 4-4: One measurement at array position (4, 5) was selected for data checking.

perform 2D SAFT to the concrete specimen.

First, a single measurement at grid position (4, 5) was selceted for data checking. The position (4, 5) is right above the bigger Styrofoam ball (ball 1) and thus is a good divice position to start with. Then three source and receiver pairs are activated, which are - in the order of "(source number, receiver number)" - pairs (1, 2), (8, 9), and (15, 16). The selection of array position and source and receiver pairs are shown in Figure 4-4.

For the selected three A-scans, SAFT reconstruction was performed and their concentric semicircles are clearly distributed at the positions corresponding to their aperture position, as shown in Figure 4-5. It is noticeable that the energy from the trace (1, 2) (on the left) is stronger than that from the other two traces. This phenomenon could be a result of side wall reflections, as trace (1, 2) is close to the side wall of the specimen and lots of energy could be reflected back to the receiver.

Then, as presented in Figure 4-6, a band-pass filter with the lower and upper cutoff frequency at 0 and 140 kHz was applied to the data set to suppress the high frequency noises.

After the implementation of the band-pass filter, the B-scan of the data set was checked. In order to visualize the reflection from a deeper position, a gain function was designed manually, as in Figure 4-7. Then the B-scan in Figure 4-8 is presenting more information at depth, for example, the backwall reflection at a recording time of about 3×10^{-4}, the direct wave is clear as the earliest arrival diagonal signal, together with the signal parallel to it being the side wall reflection, which is propagating at the speed of the direct wave.

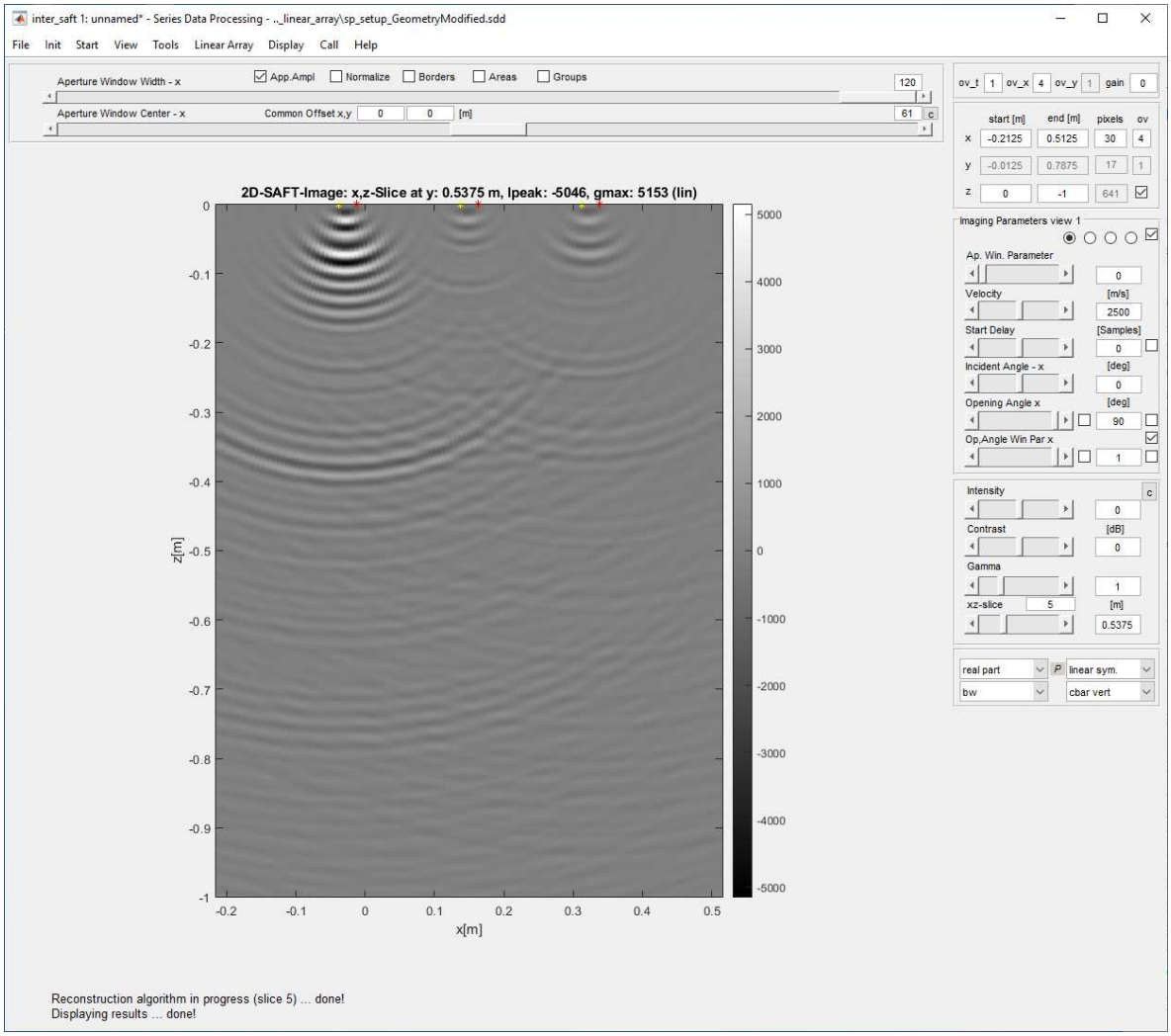

Figure 4-5: 2D SAFT reconstructions ot three A-scans selected in Figure 4-4 are shown in the same plot. It is clear that the A-scan on the left has the largest amplitude, which is anticipated to be caused by the energy reflected by the side wall of Pk264.

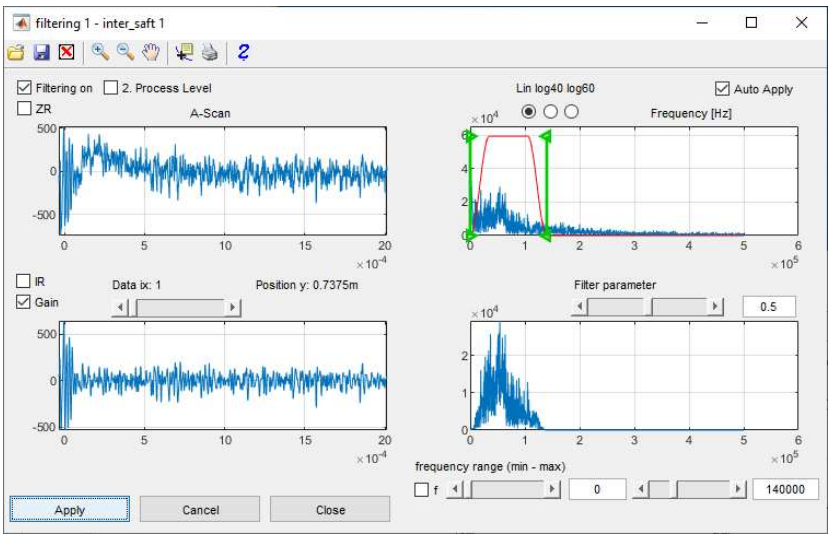

Figure 4-6: A Band-pass filter with cutoff frequencies at 0 and 140 kHz. Some high-frequency noises are filtered out, improving the S/N ratio for further processing.

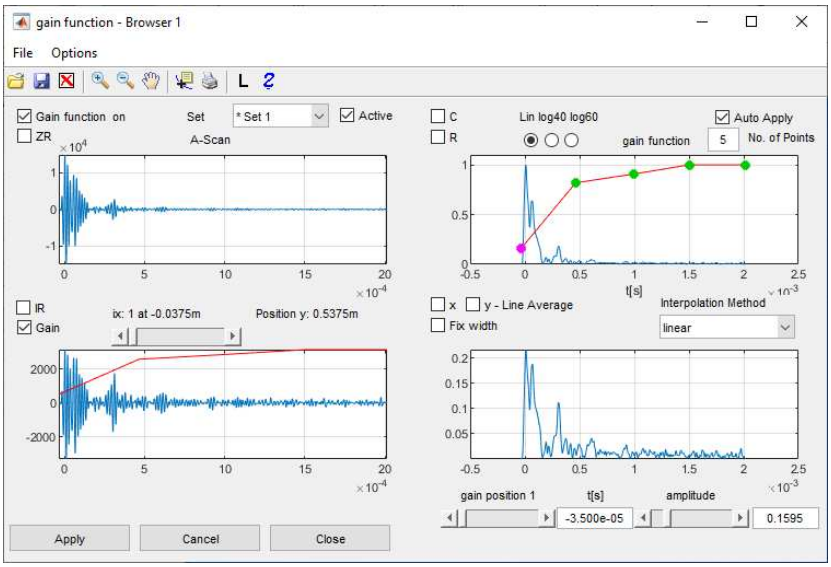

Figure 4-7: A gain function was applied to suppress the shallow arrivals and visualize more details from larger depths.

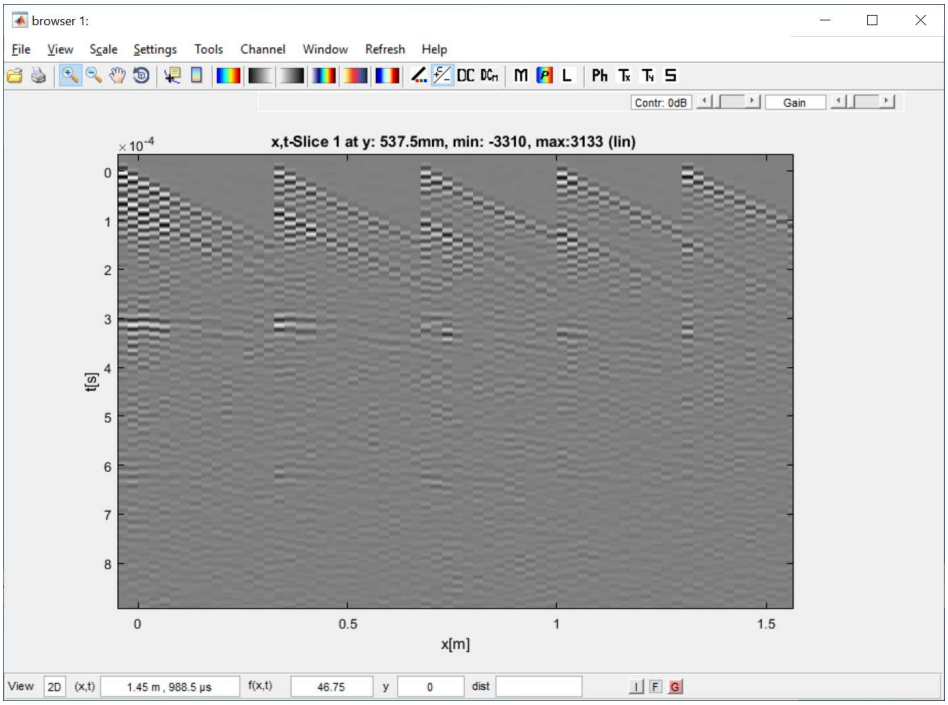

Figure 4-8: After the band-pass filter and gain function are implemented, signals from structures in the specimen are more visually recognizable. For example, the reflection at about 3×10^{-4} s is clear, which is interpreted as the signal reflected from the backwall of Pk264.

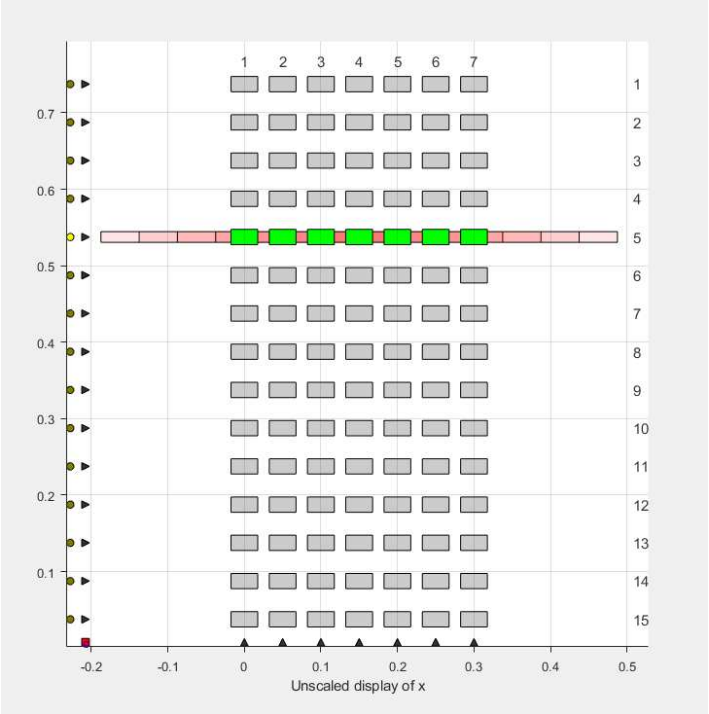

Figure 4-9: The row of measuring positions for 2D SAFT, with the extended geometry due to the aperture of the device.

4-2-2 2D SAFT

After the examination of A-scans, filter parameters, and B-scans, the 2D SAFT was finally carried out along the entire measuring line at row 5 (over styrofoam ball 1)and row 11 (over ball 6), as shown in Figure 4-9.

4-2-3 3D SAFT

First, similar to what was performed in 2D SAFT, the measurements in a single line (row 5) were selected to perform 3D SAFT in a relatively narrow area, with only 675 $mm \times 75$ mm in size. The same as performed in 2D SAFT, a band-pass filter at 0-140 kHz was applied to suppress high-frequency noise.

Then, data recorded from all the measurement points, i.e., all the device positions, was used for 3D SAFT reconstruction. As the energy contribution from every A-scan was calculated and redistributed to every target image position and each measurement contains 2016 traces of A-scans, 3D SAFT requires a longer period of time to process. For the data set used here, with $7 \times 15 = 105$ measurement positions, it took the software InterSAFT almost 7 minutes to finish the reconstruction on the personal working Laptop at BAM, while this procedure in 2D SAFT only lasted for a few seconds.

In between the single-row reconstruction and the reconstruction executed with the whole data set, certain numbers of measurement positions were selected to examine how data recorded at

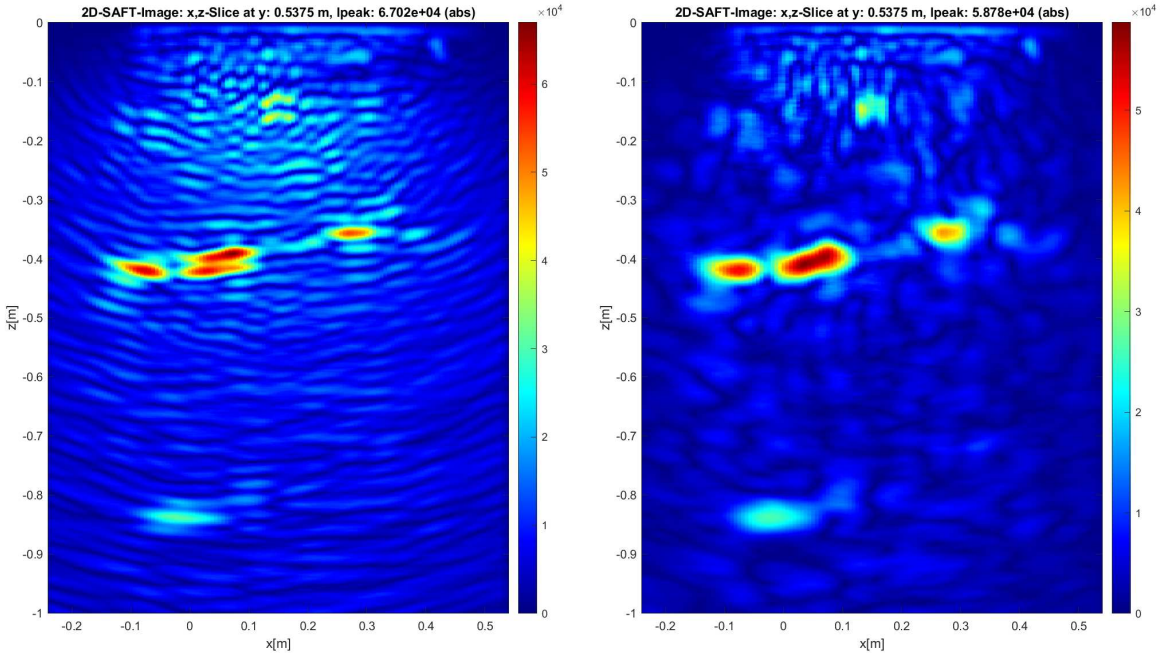

Figure 4-10: The 2D SAFT reconstructions at measuring row 5 (a)with and (b)without a band-pass filter applied at 0-140 kHz. This x-z slice is right crossing styrofoam ball 1.

different distances from the target object (the styrofoam ball) influenced the reconstruction result (see appendix).

Except for x-z slices, two x-y slices of the 3D SAFT reconstruction approximately at depth of the surface of the styrofoam balls were also produced to check the position of the styrofoam balls.

4-3 Results

4-3-1 2D SAFT

The results of 2D SAFT reconstruction are shown in Figure 4-10 and Figure 4-11. It is obvious in both figures that with the help of a band-pass filter at 0-140 kHz, the noise fringes are effectively eliminated and the imaging is depicting the structures in the specimen at more accurate position.

In Figure 4-10, the area with the energy stronger that the surroundings at x = 0.15 m, z = - 0.15 m is interpreted as the location of the styrofoam ball 1, as the position is consistent with its actual geometry.

The red area with strong energy at about x = -0.1 m should be the corner reflections, which is the signals reflceted in the coener area and then received by the sensors. The x and z coordinate of this energy area, at about (-0.1 m, -0.4 m) is well corresponding to the location of the corner of Pk264, as the corner echos are usually presented slightly shallower than their real depth (0.38 m in this case). The other high-energy area approximately at z = -0.39, x

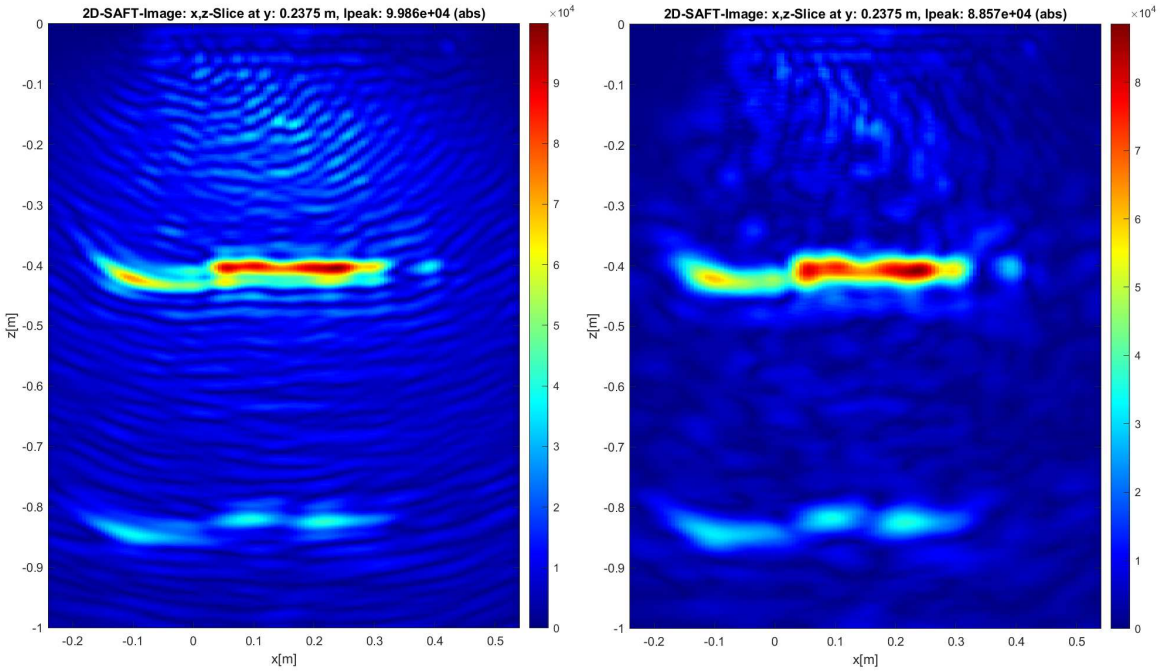

Figure 4-11: The 2D SAFT reconstructions at measuring row 11 (a)with and (b)without a band-pass filter applied at 0-140 kHz. This x-z slice is right crossing styrofoam ball 6.

from 0 to 0.15 and at 0.3, is recognized as the backwall reflection. The reasong that these two areas are not connected is that the signals are reflected by styrofoam ball 1 over the backwall, which produces a "shadow zone" blocking the signals to reach the backwall right behind the ball.

Compared to ball 1, the backwall reflection is more horizontal and continuous when viewed from Figure 4-11. The size difference between these two balls is the reason for this. Ball 1 was obstructing more signals from incidence to the backwall and the backwall reflection was not continuous because Ball 1 had an 80 mm diameter whereas Ball 2 only had a 50 mm diameter. However, ball 2's ability to reflect energy is limited, resulting in a weakened but still present backwall reflection behind it.

4-3-2 3D SAFT

The results of 3D SAFT reconstruction B-scan along row 5 (over styrofoam ball 1) and row 11 (over Ball 6) are shown in Figure 4-12. In these two images, the reconstructions were only implemented using the data acquired in the same measurement row. The 3D SAFT performed based on the whole data set reconstructed at row 5 and row 11 are displayed in Figure 4-13.

It is obvious that the resulting B-scan becomes more chaotic the more data it is based on during reconstruction. An operation frequency that is too high for the specimen could be the cause of this phenomenon. A 75 kHz operating frequency was used for the experiments

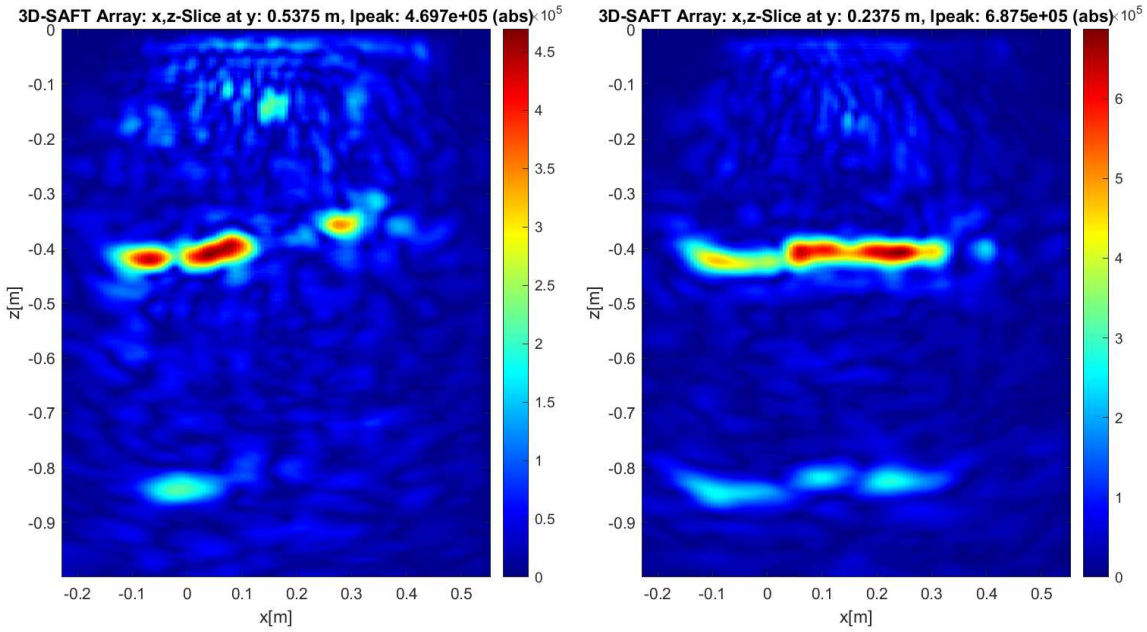

Figure 4-12: The 3D SAFT reconstructions at (a)measuring row 5 and (b)measuring row 11 with a bandpass filter applied at 0-140 kHz. The data used for 3D SAFT is from measurement row 5 and 11 respectively. This x-z slice is right crossing styrofoam ball 1 and 2.

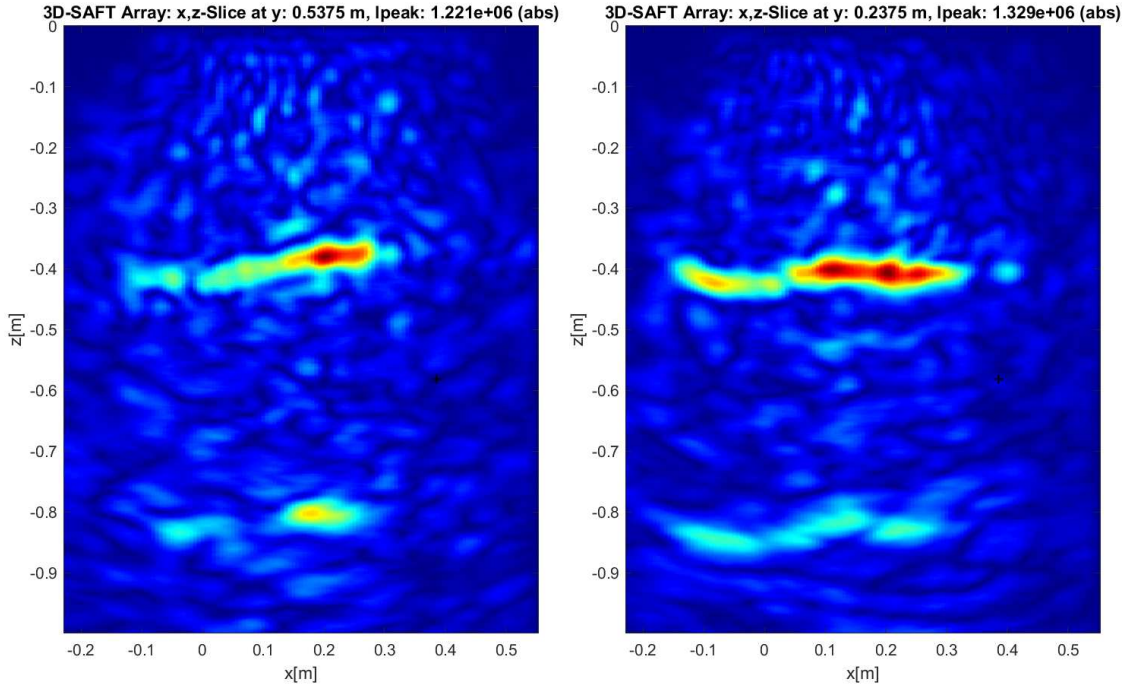

Figure 4-13: The 3D SAFT reconstructions at (a)measuring row 5 and (b)measuring row 11 from the entire data set, with a bandpass filter applied at 0-140 kHz.

conducted in this chapter. The ultrasonic wave's wavelength is

$$\lambda = \frac{v}{f} = \frac{2700\ m/s}{75000\ Hz} = 0.036\ m = 36\ mm\ ,$$

which is the same as the magnitude of the concrete aggregates. As a result, the signal is easily scattered and dispersed through propagation, further attenuating and contaminating the A-scans at longer times. The contributing energy from these A-scans is distributed for image positions farther away from the receiver position itself.

By contrasting the outcomes of 3D SAFT in Figure 4-12 with those of 2D SAFT in Figure 4-10 and Figure 4-11, we can conclude that both techniques produced 2D imaging with comparable accuracy and spatial resolution. The 3D SAFT based on the entire data set was unable to carry out its specialized function to improve the image quality because of the attenuation effect detailed in this subsection. Conversely, the results are becoming more noisy due to the high noise level coming from the distant traces.

Figure 4-14 and Figure 4-15 present the x-y slices of the 3D SAFT reconstruction at z = -158 mm. Ball 1 is represented by the red circle, and Ball 6 by the white circle. These two x-y slices were reconstructed using different amounts of data; the second was generated using the full data set, while the first was based only on the data set collected close to the ball positions. In these two x-y slices, the energy reflected from Ball 1 is more visible than that from Ball 6, which is reasonable as the diameter of Ball 1 is 80 mm, larger than the diameter of Ball 6 that is just 50 mm. In addition, in Figure 4-14, the reflections from Ball 6 is surrounded by stronger scattered noise. Then in Figure 4-15, it is also obvious that the entire image is highly influenced by noise, making the energy reflected from the two styrofoam balls hard to be identified.

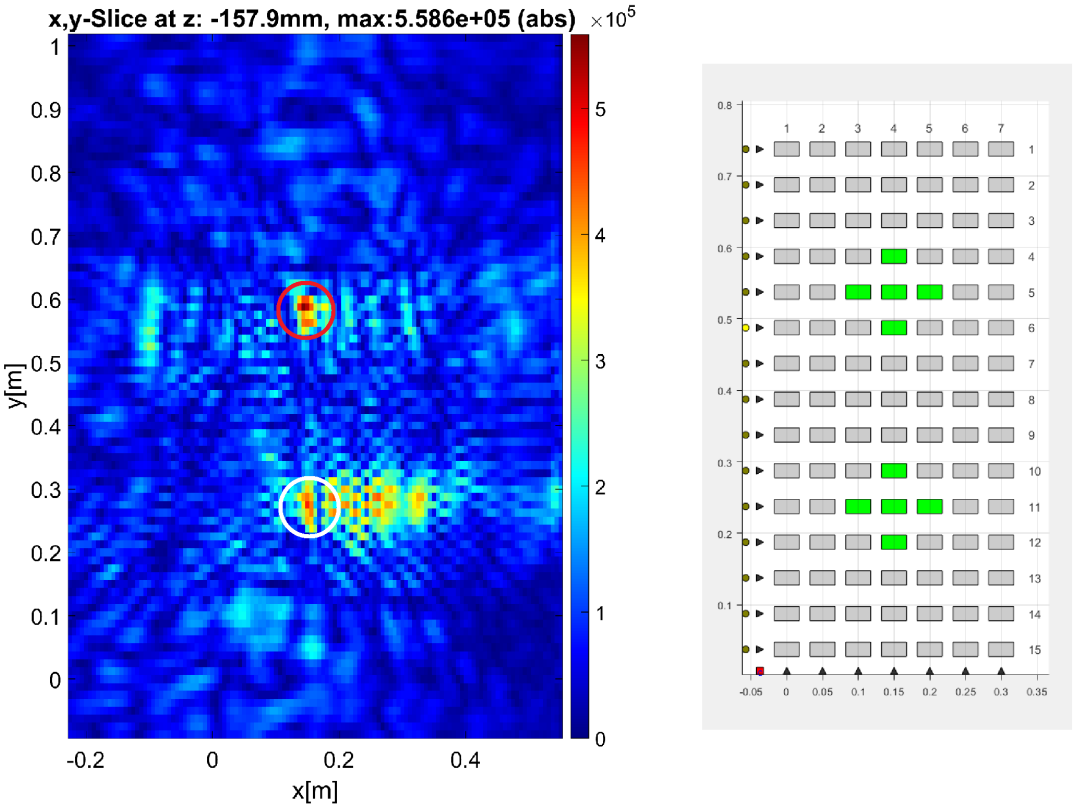

Figure 4-14: (a)x-y slice of the 3D SAFT reconstructions at the depth of z = - 158 mm, and (b)the measurement positions where the data was used for 3D SAFT reconstruction. Red circle denotes ball 1 and white circle denotes ball 6. Only a limited data set near the position of the balls were used.

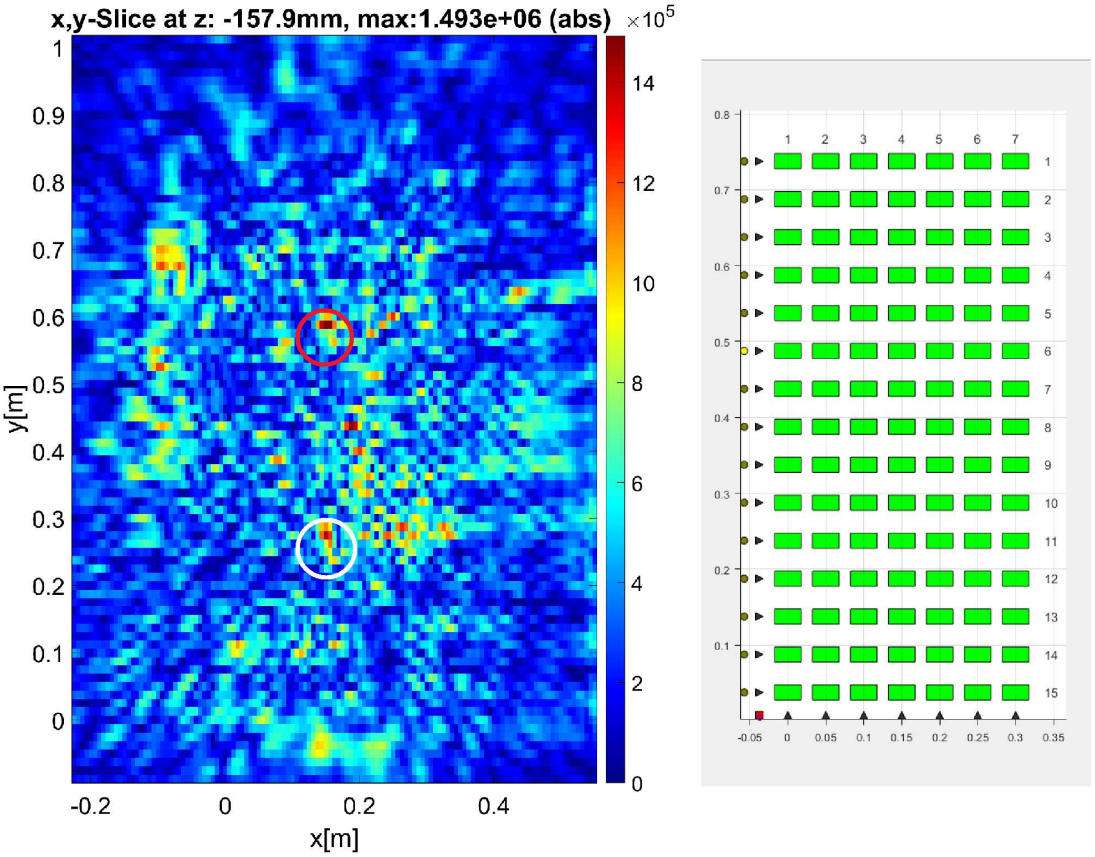

Figure 4-15: (a)x-y slice of the 3D SAFT reconstructions at the depth of z = - 158 mm, and (b)the measurement positions where the data was used for 3D SAFT reconstruction. Red circle denotes ball 1 and white circle denotes ball 6. The entire data set were used for 3D SAFT reconstruction.

Chapter 5

Discussion

The low-frequency pulse-echo ultrasonic tomography device ACS A1040 MIRA 3D PRO is gaining popularity for concrete detection due to its capabilities in localizing reinforcement rebars, detecting material voids, and measuring thickness. However, its full capabilities and limitations require independent examination and characterization, including assessing improvements in imaging resolution, inspection range, flaw detectability, and the effectiveness of the three-dimensional Full Matrix Capture/TFM method. However, its full capabilities and limitations require independent examination and characterization. Key questions include assessing imaging resolution, inspection range, flaw detectability, and the effectiveness of the three-dimensional Full Matrix Capture/TFM method.

Ultrasonic pulse-echo (UPE) testing is a highly practical and viable non-destructive testing (NDT) technique for concrete detection. It offers advantages such as fast measuring speed, high accuracy, versatility, and cost-effectiveness. The mechanical wave theory serves as the foundation for the UPE method's physical principles and is also the source of seismic detection methods. As a result, the principles and techniques used in one field by seismics and ultrasonics can be appropriately adapted and applied in another.

Significant advancements have been made in ultrasonic echo instrumentation for concrete testing over the past two decades. These instruments, often using shear wave point contact transducers, have been developed to enhance power, sensitivity, data retention, directionality, and averaging. Some devices feature linear arrays or tomographs with multiple transducer arrays, allowing for multiple measurements in a single operation. Nonetheless, for larger investigation areas or complex testing tasks, combining multiple measurements is still necessary.

In chapter 3, a mode comparison was done to ensure that the data from MIRA 3D PRO has good consistency and is compatible with the linear devices. The properties of the data acquired in both linear and matrix modes were checked. The B-scan comparison yields an intriguing result: the target concrete's structure is eliminated when the two modes' data are subtracted from one another. This indicates that the data from both modes is fairly comparable, allowing for linear processing and analysis using Matrix Mode data.

Even so, the outcome of the A-scan comparison is not what was anticipated, with the results of both mode comparisons indicating that there may be some errors in the A-scan comparison, especially in the data sorting process. As there are 120 traces in one measurement for Linear Mode and 2016 traces for Matrix Mode, and the device position is also moving along the aperture, mistakes about data sorting and trace selection are easy to occur. For future research on this device, A-scan comparisons between data in Linear and Matrix Modes are suggested to be carried out. If possible, it would also benefit if the data from A1040 MIRA 3D PRO was compared to that from its predecessor, A1040 MIRA, to have a close look at whether and how the signals transmitted and received by the sensors were improved.

In Chapter 4, 2D and 3D SAFT were carried out on a specimen with 3D anomaly objectives mounted inside. With the help of SAFT, the location and geometry of the objectives are reconstructed at their true positions so that we can obtain more information from the tested concrete based on the existing data set. In the experiments in this chapter, the operation frequency was set too high so that the signal attenuates sharply with propagation, limiting its ability to bring information from a greater distance and thus also increasing the noise level of the final image. Because the signal is contaminated by noise, the superposition algorithm of 3D SAFT did not constructively increase the desired elements. On the other hand, it increased the noise level so that the target structure was less visible. As a result, the reconstruction results of 3D SAFT did not show much improvement compared to those of 2D SAFT. For further research on 2D and 3D SAFT based on the data measured by MIRA 3D, it is recommended to conduct an operation frequency calibration before measurements on a certain concrete specimen, finding the optimal frequency to present a better reconstruction result.

The experiments in this chapter were performed on a part of a concrete specimen where there were no rebars or other structures. For further experiments on the MIRA 3D PRO, on 3D SAFT, or on the total focusing method/full matrix capture technique, specimens with more complicated structures are also recommended.

For further studies on the properties and parameters of MIRA 3D PRO, the function of so-called E-boosting is also suggested to be tested, which is claimed to have utilized "innovative transmitting principles" to increase the signal's energy.

In addition, the algorithm of 3D SAFT calculates the contribution of all the A-scans to each image point, which means that this procedure requires a large amount of time. The experiment in Chapter 4 has already given a glance at the difference in the calculation speed in 2D and 3D SAFT. Following experiments and research, the trade-off between better image quality and being less time-consuming should also be taken into account.

Bibliography

[ACS, 2018] (2018). A1040 mira. https://acs-international.com/product/a1040-mira/. Accessed: 2023-10-25.

[ACS, 2022a] (2022a). A1040 mira 3d pro. http://acs-international.com/instruments/ultrasonic-pulse-echo-tomography-systems-mira/a1040-mira-3d-pro/. Accessed: 2023-06-14.

[ACS, 2022b] ACS (2022b). *A1040 MIRA 3D: Ultrasonic low-frequency tomograph - Operation manual*. Acoustic Control Systems – ACS Group, Saarbrücken, Germany.

[Ahmad et al., 2014] Ahmad, N., Rahim, R., Rahim, H., and Rahiman, M. (2014). A review of ultrasonic application on non-destructive testing method for concrete structure. *J. Teknol*, 70:112–119.

[Ashton et al., 1993] Ashton, C. P., Bacon, B., Mann, A., Moldoveanu, N., Déplanté, C., Aquitaine, E., Sinclair, T., Redekop, G., and AS, M. O. Q. (1993). 3d seismic survey design. *The Leading Edge*, 12(11):1094–1117.

[FPrimeC, 2017] FPrimeC (2017). Ultrasonic testing of concrete. https://www.fprimec.com/ultrasonic-testing-of-concrete/. FPrimeC Solutions Inc.

[Jain et al., 2021] Jain, H., Patankar, V., and Kulkarni, M. (2021). Ultrasonic testing of concrete structures: a review.

[JAIN and Patankar, 2019] JAIN, H. and Patankar, V. H. (2019). Advances in ultrasonic instrumentation for inspection of concrete/rcc structures.

[Maack et al., 2023] Maack, S., Küttenbaum, S., Bühling, B., Borchardt-Giers, K., Aßmann, N., and Niederleithinger, E. (2023). Low frequency ultrasonic pulse-echo datasets for object detection and thickness measurement in concrete specimens as testing tasks in civil engineering. *Data in Brief*, page 109233.

[Mayer and Cinta, 2012] Mayer, K. and Cinta, P. (2012). *User Guide of Graphical User Interface inter SAFT*. University of Kassel, Department of Computational Electronics and Photonics.

[Mayer et al., 2008] Mayer, K., Langenberg, K.-J., Krause, M., Milmann, B., and Mielentz, F. (2008). Characterization of reflector types by phase-sensitive ultrasonic data processing and imaging. *Journal of nondestructive Evaluation*, 27:35–45.

[Niederleithinger et al., 2019] Niederleithinger, E., Maack, S., Mielentz, F., Effner, U., and Strangfeld, C. (2019). Review of recent developments in ultrasonic echo testing of concrete. In *5th International Conference on Smart Monitoring, Assessment and Rehabilitation of Civil Structures*, Potsdam, Germany. https://www.ndt.net/?id=24886.

[Niederleithinger et al., 2017] Niederleithinger, E., Popovic, J. S., Clauser, C., and Große, C. (2017). Seismic methods applied to ultrasonic testing in civil engineering. Technical report, Rheinisch-Westfälische Technische Hochschule Aachen.

[Popovics, 2005] Popovics, J. S. (2005). Ultrasonic testing of concrete structures. *Materials evaluation*, 63(1).

[Popovics and Rose, 1994] Popovics, J. S. and Rose, J. L. (1994). A survey of developments in ultrasonic nde of concrete. *IEEE transactions on ultrasonics, ferroelectrics, and frequency control*, 41(1):140–143.

[Schickert, 2005] Schickert, M. (2005). Progress in ultrasonic imaging of concrete. *Materials and Structures*, 38:807–815.

[Schickert et al., 2003] Schickert, M., Krause, M., and Müller, W. (2003). Ultrasonic imaging of concrete elements using reconstruction by synthetic aperture focusing technique. *Journal of materials in civil engineering*, 15(3):235–246.

[SEG, 2014] SEG (2014). Kirchhoff migration in practice. https://wiki.seg.org/wiki/Kirchhoff_migration_in_practice. SEG Wiki.

[SEG, 2020] SEG (2020). Reflection coefficient. https://wiki.seg.org/wiki/Reflection_coefficient. SEG Wiki.

[Wu, 2023] Wu, D. (2023). Method review for ultrasonic echo testing applied in concrete. Technical report, final report for course Research Module, RWTH Aachen.

Appendix A

A-1 Codes and Scripts

A-1-1 An appendix subsection with Python Lisitng

```
"""
Created on Wed Sep 27 16:52:37 2023

@author: dwu2

Description: A-Scan comparison
"""

#### export to sgy-format
from IPython import get_ipython
get_ipython().magic('reset -sf')  #close all figures and delete variables
get_ipython().run_line_magic('matplotlib', 'qt') #plot figures in extra window

#packages
# import struct
import matplotlib.pyplot as plt
import numpy as np
# import scipy as sc
import os
import pandas as pd

#seismic specific
import obspy
from obspy import read, Trace, Stream, UTCDateTime
from obspy.core import AttribDict, Stats
from obspy.io.segy.segy import SEGYTraceHeader, SEGYBinaryFileHeader
from obspy.io.segy.core import _read_segy
```

```
ns = 2175 #number of samples per trace
dt = 1e-6 #sampling interval in second


u_lin = np.load('u_lin_89(08-13).npy')
u_mat_1 = np.load('u_mat_(8,1)(13,1).npy')
u_mat_2 = np.load('u_mat_(8,2)(13,2).npy')
u_mat_3 = np.load('u_mat_(8,3)(13,3).npy')
u_mat_4 = np.load('u_mat_(8,4)(13,4).npy')


u_lin = u_lin[0:ns]
u_mat_1 = u_mat_1[0:ns]
u_mat_2 = u_mat_2[0:ns]
u_mat_3 = u_mat_3[0:ns]
u_mat_4 = u_mat_4[0:ns]
u_lin = u_lin - np.mean(u_lin)
u_mat_1 = u_mat_1 - np.mean(u_mat_1)
u_mat_2 = u_mat_2 - np.mean(u_mat_2)
u_mat_3 = u_mat_3 - np.mean(u_mat_3)
u_mat_4 = u_mat_4 - np.mean(u_mat_4)

norm_lin = np.linalg.norm(u_lin)
norm1 = np.linalg.norm(u_mat_1)
norm2 = np.linalg.norm(u_mat_2)
norm3 = np.linalg.norm(u_mat_3)
norm4 = np.linalg.norm(u_mat_4)

u_lin = u_lin/norm_lin
u_mat_1 = u_mat_1/norm1
u_mat_2 = u_mat_2/norm2
u_mat_3 = u_mat_3/norm3
u_mat_4 = u_mat_4/norm4

u_mat_avg = (u_mat_1 + u_mat_2 + u_mat_3 + u_mat_4)/4

###################### A-Scan Plotting ############################
fig1,ax1 = plt.subplots(figsize=(10,6)) #handle
# t = np.arange(0, ns*dt, dt)
# z = t*v/twt # Two way travel time
plt.plot(u_lin, label='Linear Mode',linewidth=1.5, color='k') # plot A-Scan
# plt.plot(u_mat_avg, label='Matrix Mode 1',linewidth=1.5, linestyle='--')
plt.plot(u_mat_1, label='Matrix Mode 1',linewidth=1.0, linestyle='--')
plt.plot(u_mat_2, label='Matrix Mode 2',linewidth=1.0, linestyle='--')
plt.plot(u_mat_3, label='Matrix Mode 3',linewidth=1.0, linestyle='--')
plt.plot(u_mat_4, label='Matrix Mode 4',linewidth=1.0, linestyle='--')
```

```python
# plt.plot(t, u_trace_select,color='k') # plot A-Scan with time
# plt.title('A-Scan Comparison Between Linear and Matrix Modes No. %s' %No_Ascan)
plt.ylabel('Normalized Amplitude')
plt.xlabel('Sample')
leg = plt.legend()
# ax1.set_xlim([0,max(z)])
plt.show()
```

A-1-2 A Matlab Listing

```matlab
%%%%%%%%%%%%%%%%%%%%%%%%%%%%%%%%%%%%%%%%%%%%%%%%%%%%
% This script is written to plot the B-scan comparisons
%   from the data acquired by ACS A1040 MIRA 3D PRO
% Author: Wudi
% Created on 12. Jun. 2023
% Last modified on 27. Oct. 2023
%%%%%%%%%%%%%%%%%%%%%%%%%%%%%%%%%%%%%%%%%%%%%%%%%%%%%

clc
clear workspace
close all

load sp_setup_rec2d_0-2m_extr.mat  % linear mode data
lin_mode = real(squeeze(U.data));
load combined_linear_array_rec2d_0-2m_extr.mat
% linear data compressed from matrix data
lin_comp = real(squeeze(U.data));
load full_matrix_rec3d_0-2m_extr.mat  % matrix data
mat_mode = real(squeeze(U.data));

lin_mode_nor = normalize(normalize(lin_mode),2);
lin_comp_nor = normalize(normalize(lin_comp),2);
mat_mode_nor = normalize(normalize(mat_mode),2);
differnce_lin_lin = lin_mode_nor - lin_comp_nor;
% sum_lin_lin = lin_mode + lin_comp;

figure
subplot(2,2,1)
imagesc([0 2000],[],lin_mode_nor')
colormap(gray);
colorbar
title('Lnear Mode');
xlabel('Distance / mm');
% ylabel('Time series');

subplot(2,2,2)
imagesc([0 2000],[],lin_comp_nor')
colormap(gray);
colorbar
title('Matrix Mode Compressed to Linear Dataset');
xlabel('Distance / mm');


subplot(2,2,3)
imagesc([0 2000],[],mat_mode_nor')
colormap(gray);
colorbar
title('Matrix Mode');
xlabel('Distance / mm');

subplot(2,2,4)
imagesc([0 2000],[],differnce_lin_lin')
colormap(gray);
colorbar
title('Difference between Linear Mode and Matrix Compressed to Linear');
xlabel('Distance / mm');
% % caxis([-2000 2000]);
% subplot(2,3,5)
% imagesc(sum_lin_lin')
```

Appendix B

B-1 A Brief Manual on MIRA 3D and InterSAFT

Based on the working experiences with the hardware ACS A1040 MIRA 3D PRO and the software InterSAFT, I wrote a brief Mnual on MIRA 3D and InterSAFT to help readers get started quickly. The Manual is shown below.

Measurement

- Press the **power button** for 3 sec to activate the device.
- Switch on the controlling smartphone, open the **MIRA 3D app**.
- Tap **Setting → Wi-Fi**, select MIRA 3D to connect with the two basic units.
- Set the parameters for measurement, incl. Central frequency, analog and digital gain, working mode (linear/matrix).
- Tap **A-Scan** for pre-checking. Modify **analog gain** to keep the amplitude in the received range.
- Tap Map, enter the Map mode, to start with the measuring (check the parameters on the right before, incl. x and y interval)
- Put MIRA 3D on the measuring position, press the entire device vertically towards the target surface (when the device is cocntacting the surface, make sure not to move the device along the surface, otherwise the tips of the sensors will be damaged)

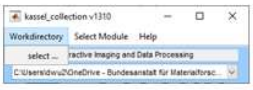

(Select the folder with config.m3d)

1. Kassel_collection_v1310.exe
2. Workdirectory → select …
3. Select Module → script calculation →
4. Select InterSaft/application_v1310/scripts/**convert_all_v2.m**
   to convert .bin data into .ghk data
5. Change the script: Mode = 3 for conversion to normal linear mode
   Mode = 4 for matrix mode
6. Start Calculation → Close (when finished)

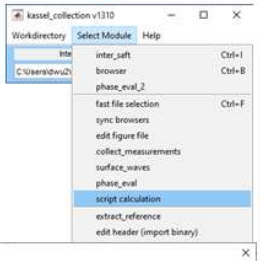

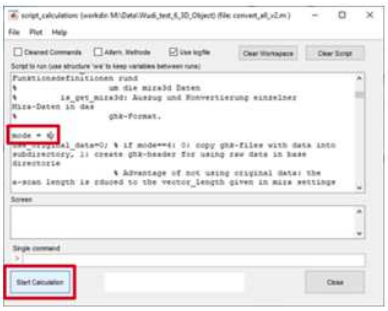

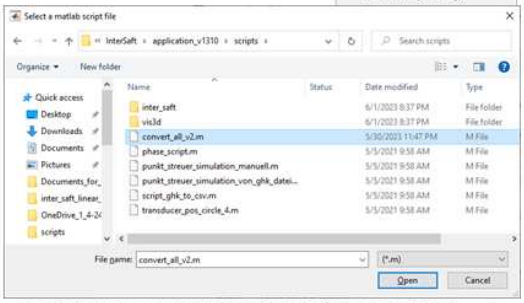

7. Change Work directory (as in step 2.) to the folder **inter_saft_linear_array** (or **inter_saft_matrix_array)**
8. Select Module → inter_saft → **select_preset** window appears → Standard preset (or MIRA 3D)
9. Appears the **inter_saft 1** window. Linear Array → Series Definition (for geometery defining)

10. In the is_series_processing window, **File → Load First Datafile (.ghk)**

    Select the first file (with "1_1" in the filename)
11. Pops up the Numbering window, Column sequences first. Then the geometry information is imported.

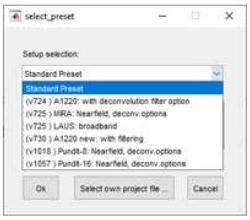

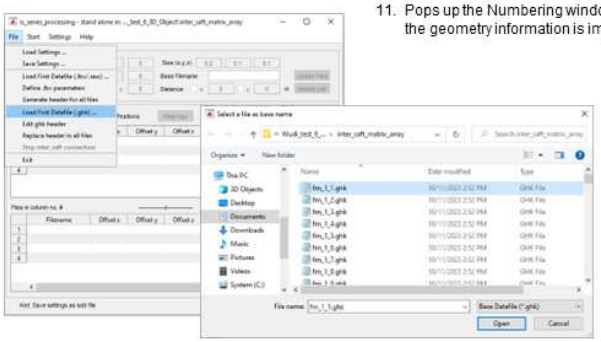

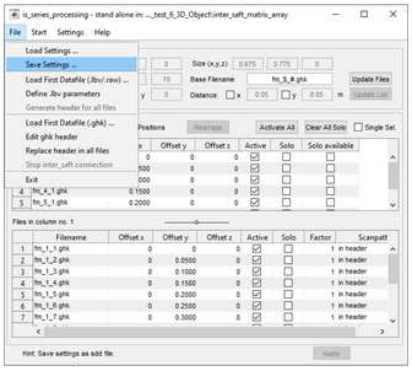

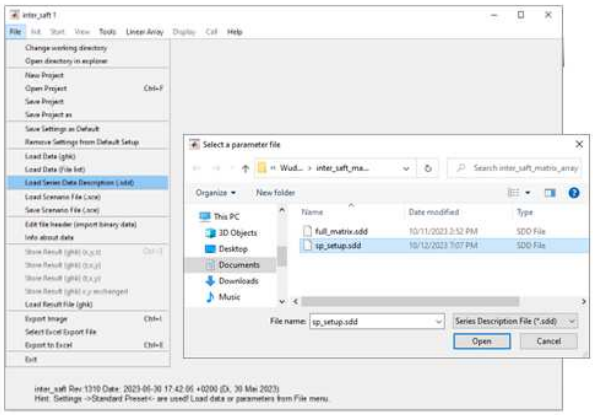

12. In the *is_series_processing* window: File → Save Settings → Exit (to save the geometry setting).
13. In the *inter_saft 1* window: File → Load Series Data Description (.sdd) → choose sp_setup.sdd just saved.
14. Then the *range_definition* window appears, usually no changes in this window: **Start**.

12. Then the new *inter_saft 1* window appears: Init → Initialize Parameters
13. In the popped up window *parameter_selection*: set velocity, Center Frequency, and extension of the plotting area (note: the units for x- and y-extension are the number of delta x and delta y) → OK.
14. **Start** → Start homogeneous SAFT.

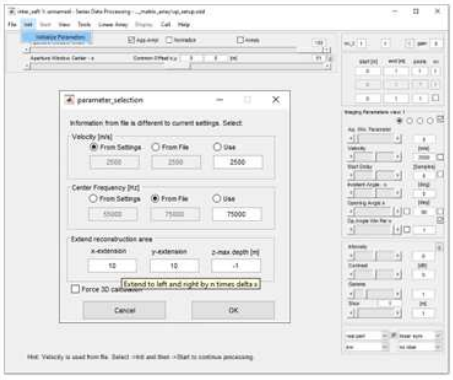

Thank you for reading.

Contact:

Di Wu (Wudi)

Email: wudi1793@gmail.com

www.bam.de